Journal of Marine Science and Technology

Volume 32 | Issue 1 Article 7

Elimination of Noise in a Ship Cabin Using Multi-layered Acoustic Boards: An APSO and SA Approach

Min-Chie Chiu
Department of Mechanical and Materials Engineering, Tatung University, Taiwan, ROC, mcchiu@gm.ttu.edu.tw

Ho-Chih Cheng
Department of Information Technology, Ling Tung University, Taiwan, ROC

RESEARCH ARTICLE

Elimination of Noise in a Ship Cabin Using Multi-layered Acoustic Boards: An APSO and SA Approach

Min-Chie Chiu [a,*], Ho-Chih Cheng [b]

[a] Department of Mechanical and Materials Engineering, Tatung University, Taiwan, ROC
[b] Department of Information Technology, Ling Tung University, Taiwan, ROC

Abstract

A high level of noise, combined with pure tones, is often encountered in ship's cabins, leading to severe psychological and physiological issues for the crew. To address this problem, an indoor noise abatement solution becomes necessary that utilizes efficient acoustic boards integrated with resonators, positioned along the inner walls of the cabin. However, the thickness of the acoustic boards must be strictly limited due to maintenance and operational considerations. This limitation results in insufficient sound absorption capabilities and a restricted range of tuned frequencies, as the resonating frequency of a standard Helmholtz resonator is closely tied to its cavity. A modified Helmholtz resonator with an internally extended resonating tube is adopted to overcome this drawback. This modification saves space while maintaining the same tuning effect. Two types of acoustic boards are proposed in this study: acoustic board A, which consists of a one-layered acoustical board and an extended Helmholtz type resonator, and acoustic board B, which includes a two-layered acoustical board and an extended Helmholtz type resonator. An accuracy check of the modified Helmholtz resonator is conducted using experimental data before proceeding with the optimization of the acoustic boards. Additionally, a sensitivity analysis is performed to evaluate the impact of the geometric parameters of the acoustic boards. Two bionic algorithms, namely *APSO* (Accelerated Particle Swarm Optimization) and *SA* (Simulated Annealing), are employed to achieve an optimal design. The results of optimization demonstrate that the *APSO* algorithm slightly outperforms the *SA* algorithm. Furthermore, acoustic board B exhibits a wider spectrum of acoustical attenuation compared to acoustic board A. Consequently, this study showcases the effective reduction of noise in an enclosed machine cabin using *APSO* and *SA*, while taking into account the constraint of limited thickness.

Keywords: Multi-layer, Pure tone, Extended Helmholtz resonator, Accelerated particle swarm optimization, Simulated annealing

1. Introduction

Noise exposure prevention is important to avoid levels that will lead to complaints [1,2], and to health effects such as sleep disorders with awakenings [3], learning impairment [4], hypertension ischemic heart disease [5–7], diastolic blood pressure [8,9], reduction of working performance [10,11], or annoyance [12–14]. Besides acoustic energy exposure, parameters related to the sound signals like peak levels, temporal variations, amplitude modulation, impulsivity, frequency distribution, have serious impact over perception [15–22] and singular noise source should be then avoided [23].

Ships radiate sounds that can affect marine fauna or humans, depending on the underwater or airborne emissions. Underwater noise emissions of ships have been largely studied in the past and effects have been widely demonstrated [24–27]. Airborne sound emitted by moving ships were finally investigatedonly in the recent years, and it

Received 15 October 2023; revised 29 January 2024; accepted 30 January 2024.
Available online 11 March 2024

* Corresponding author at: Department of Mechanical and Materials Engineering, Tatung University, No. 40, Sec. 3, Zhongshan N. Rd., Taipei, 10452, Taiwan, ROC.
E-mail address: mcchiu@gm.ttu.edu.tw (M.-C. Chiu).

https://doi.org/10.51400/2709-6998.2733

was found to be disturbing for citizens living around the coasts, port or canal cities [28−39]. Indoor sound emissions have been widely investigated with standard, or novel techs like acoustic cameras [40−44].

Addressing the challenge of dealing with wideband sound combined with numerous tones within an enclosed machine room, Chiu [45] proposed the use of hybrid acoustic panels comprising a single-layered sound absorber and multiple Helmholtz resonators. However, as indicated in Chiu's research [45], achieving the desired resonating frequency with the standard Helmholtz resonator still requires a substantial thickness, which significantly reduces the available space for maintenance and operation. To overcome this limitation and enhance the noise reduction capabilities in a broadband sound field, a multi-layered acoustical board hybridized with a modified Helmholtz resonator is presented. Duan et al. [46] investigated the adoption of an internally extended resonating tube, which effectively reduces the resonator's capacity while maintaining a low tuned frequency. Furthermore, Chang et al. [47−49] analyzed that increasing the layers of acoustical board can enhance the wideband sound absorbing coefficient. Consequently, two types of acoustic boards are presented in the study: acoustic board A, which consists of a perforate front cover, an acoustical wool, an air gap, and an extended Helmholtz type resonator, and acoustic board B, which includes a perforated plate, a sound absorbing material, an air space, another perforated plate, another acoustical wool, an air gap, and an extended type Helmholtz resonator. These acoustic boards are employed to address a wideband noise combined with a prominent single tone. The selection of an appropriate optimizer is crucial to achieve the optimal shape design of the acoustic boards within a fixed thickness. Over the past three decades, there has been a growing interest in solving algorithmic problems by drawing inspiration from natural systems in physics and biology. Traditional gradient methods, such as the exterior penalty function (*EPFM*), the interior penalty function method (*IPFM*), and the feasible direction method (*FDM*) [50], often face limitations in exploring candidate solutions across a wide database and tend to converge to local optima. Therefore, various bionic algorithms, including the genetic algorithm (*GA*) [47,49−51], simulated annealing (*SA*) [48,52−54], and particle swarm optimization (*PSO*) [45,55,56], have been widely applied to engineering problems. In this study, both the accelerated particle swarm optimization (*APSO*) and simulated annealing (*SA*) are adopted to facilitate the optimization process with fewer control parameters. These algorithms have been found to be forceful in dealing with optimization in continuous and nonlinear problems. The research focuses on a machine room containing a root blower that emits a significant low-frequency noise combined with a pure tone at 110 Hz. Consequently, a rapid and effective method for noise reduction is presented by optimizing the design of a shaped hybrid acoustic board within the constraints of limited space.

2. Mathematical background

2.1. Acoustic board A

2.1.1. Sound absorbing coefficients of acoustic board A's dissipative part

In order to address the noise levels within a machine room that is subject to constraints (as depicted in Fig. 1-(a)), where a low-frequency noise is combined with a prominent pure tone (as detailed in Table 1), an acoustic board configuration consisting of a multi-layer acoustic board hybridized with an extended Helmholtz resonator (as illustrated in Fig. 1-(b)) is utilized. These acoustic boards are internally installed on the four walls and the ceiling of the machine room. To obtain the sound absorbing coefficient using a plane wave theory, a three-dimensional acoustic wave propagating through a quiescent medium enclosed by rigid rectangular partitions, shown in Fig. 2 is assumed. As shown in Fig. 3-(a), the acoustic board A consists of two components: a dissipative element (comprising a perforate front cover, acoustical wool, and air gap) and a reactive element (consisting of one extended Helmholtz type's resonator). Before calculating the sound absorbing coefficients associated with the dissipative part, the derivation of mathematical matrix for adjacent acoustical nodes is necessary. The related matrix expression for one-layer sound absorber's dissipative part is derived and shown in Appendix A. As derived in Appendix A, the form of the acoustic pressure p and the acoustic particle velocity u between node 0~node 1, node 1~node 2, and node 2~node 3 are given as:

$$\begin{pmatrix} p_1 \\ u_1 \end{pmatrix} = \begin{bmatrix} cos(\omega L_1/c_o) & j\rho_o \mathbf{c_o} \sin(\omega L_1/c_o) \\ j\dfrac{\sin(\omega L_1/c_o)}{\rho_o \mathbf{c_o}} & cos(\omega L_1/c_o) \end{bmatrix} \begin{pmatrix} p_o \\ u_o \end{pmatrix} \tag{1a}$$

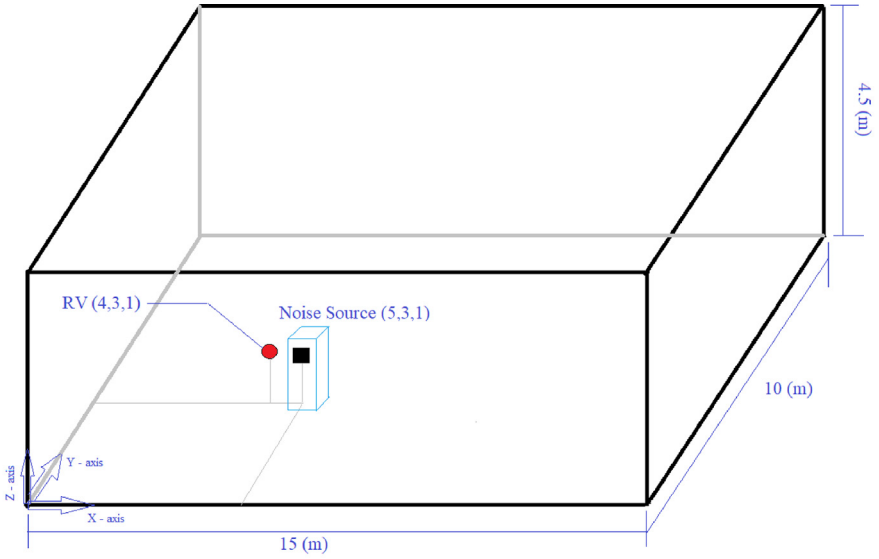

(a) without adding internally installed acoustical board

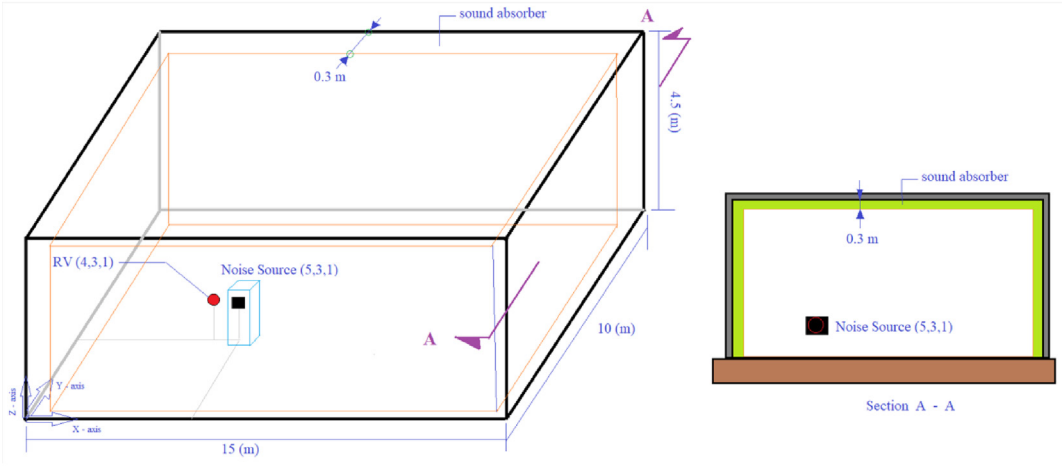

(b) with adding internally installed acoustical board

Fig. 1. A noisy equipment within a space-constrained ship's machine cabin.

$$\begin{pmatrix} p_2 \\ u_2 \end{pmatrix} = \begin{bmatrix} cos\left(k_{fiber1}D_{f1}\right) & jZ_{fiber1}\sin\left(k_{fiber1}D_{f1}\right) \\ j\dfrac{\sin\left(k_{fiber1}D_{f1}\right)}{Z_{fiber1}} & cos\left(k_{fiber1}D_{f1}\right) \end{bmatrix} \begin{pmatrix} p_1 \\ u_1 \end{pmatrix} \tag{1b}$$

Table 1. Acoustical power level of a root blower within a ship's machine room.

(1/1) Octave Band (hz)	63	110	125	250	500	1000	2000
Lw (@1m dB(A)	109	129	110	107	101	95	89

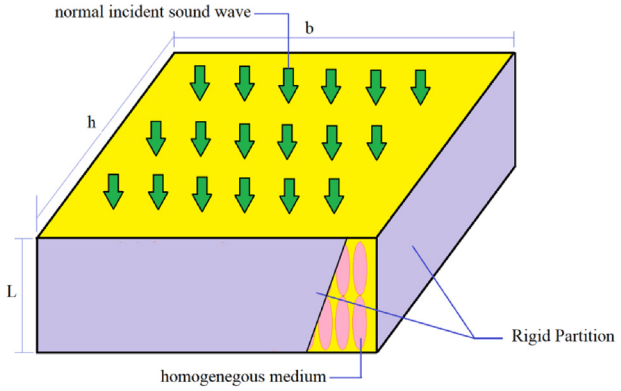

Fig. 2. For three-dimensional acoustic wave propagating through a quiescent medium (with the rectangular partitions).

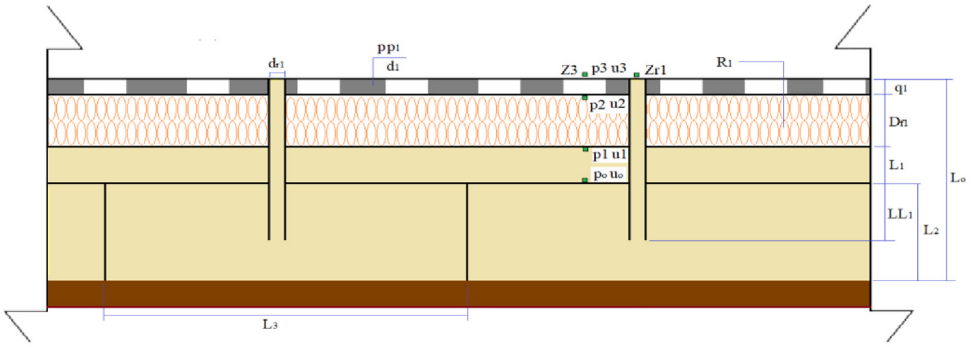

(a) Acoustic board A composed of a one-layer sound board (dissipative unit) and one extended Helmholtz resonator (reactive unit).

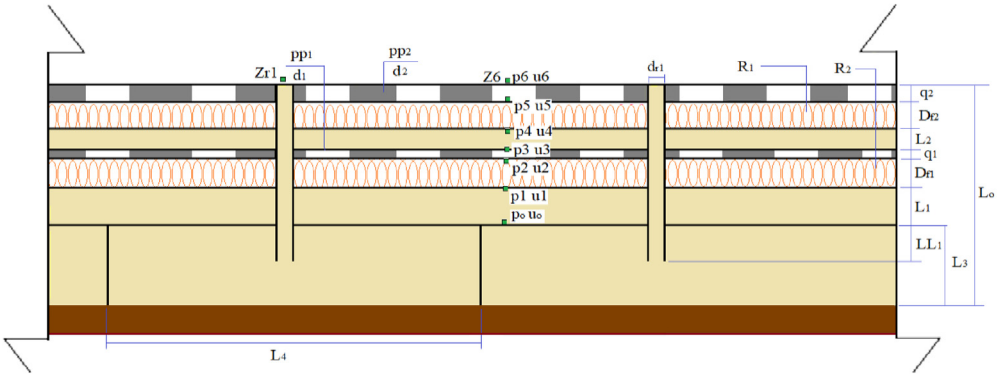

(b) Acoustic board B composed of a two-layer sound board (dissipative unit) and one extended Helmholtz resonator (reactive unit).

Fig. 3. Two kinds of acoustic boards used in the noise abatement of a space-constrained machine room.

$$\begin{pmatrix} p_3 \\ u_3 \end{pmatrix} = \begin{bmatrix} 1 & Z_{p1} \\ 0 & 1 \end{bmatrix} \begin{pmatrix} p_2 \\ u_2 \end{pmatrix} \tag{1c}$$

The specific normal impedance at point 3 is given in Eq. (2) by developing Eq. (1c)

$$Z_3 = Z_2 + Z_{p1} \tag{2}$$

Using the formula of the specific normal impedance and the wave number of the perforated plate from Beranek & Ver [57] yields

$$Z_{p1} = \frac{\rho_o}{pp_1}\sqrt{8\gamma\omega}\left(1+\frac{q_1}{2d_1}\right) + j\frac{\omega\rho_o}{pp_1}\left[\sqrt{\frac{8\gamma}{\omega}}\left(1+\frac{q_1}{2d_1}\right)+q_1+\delta_1\right] \tag{3a}$$

$$\delta_1 = 0.85(2d_1)\left(1-1.47\sqrt{pp_1}+0.47\sqrt{pp_1^3}\right) \tag{3b}$$

Here, γ is the kinematic viscosity of air, pp_1 is the perforated rate of the plate, q_1 is the thickness of the plate, and d_1 is the diameter of the plate's hole.

For normal incidence, the sound absorbing coefficient of a one-layer dissipative part [58,59] is

$$\alpha_1(f, pp_1, d_1, R_1, q_1, D_{f1}, L_1) = 1 - \left|\frac{Z_3 - \boldsymbol{\rho_o c_o}}{Z_3 + \boldsymbol{\rho_o c_o}}\right|^2 \tag{4}$$

Taking into account the impact of the contribution by using the related ratio of area between the dissipative unit and reactive unit, an equivalent averaged sound absorbing coefficient per square meter for the dissipative part can be obtained as follows:

$$\alpha_{1(avg)}(f, pp_1, d_1, R_1, q_1, D_{f1}, L_1) = \left[\alpha_1\left(L_4^2 - \frac{\pi d_{r1}^2}{4}\right) \Big/ L_3^2\right] \tag{5}$$

2.1.2. Acoustic board A's reactive part

The mechanism of the extended Helmholtz Resonator (HR), a reactive unit, is depicted in Fig. 4-(a). Assuming that the characteristic length of the

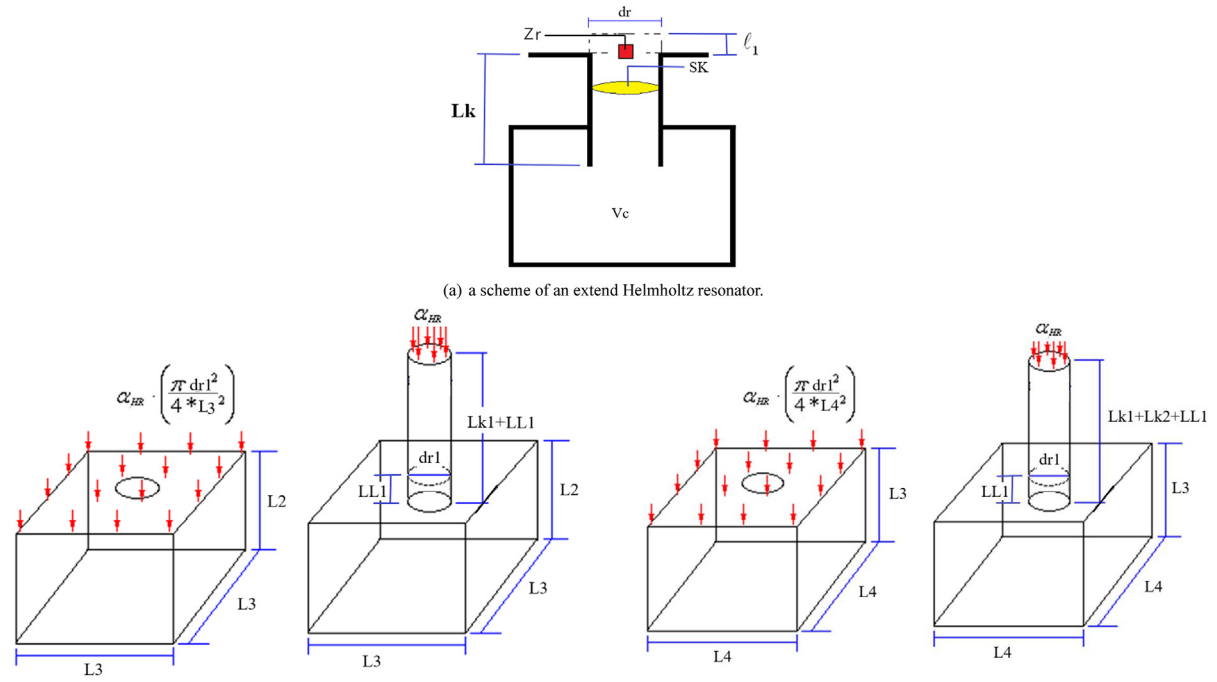

(a) a scheme of an extend Helmholtz resonator.

(b) average sound absorbing coefficient for an one-layer sound board and an extended Helmholtz resonator (acoustic board A)

(c) average sound absorbing coefficient for an two-layer sound board and an extended Helmholtz resonator (acoustic board B)

Fig. 4. An extended Helmholtz resonator imbedded with the acoustic board.

HR element is smaller than the acoustical wavelength, the neck of the resonator can be treated as a lumped mass. During the adiabatic resonating process, the compression of the air within the resonator can be analogized to a spring. Considering the acoustical end correction, the factors (ℓ_1) for the end correction with flange can be defined as [46,60]:

$$\ell_1 = \frac{8d_r}{3\pi} = 0.849r_r \tag{6}$$

For a simplified mathematical model of the *HR* element, the resonant frequency (f_{res}) is [45,46]

$$f_{res} = \frac{c_o}{2\pi}\sqrt{\frac{SK}{V_c(L_k + \ell_1)}} \tag{7}$$

Here, c_o represents the speed of sound, SK denotes the cross-sectional area of the resonating neck, L_k represents the total length of the resonating neck (including the extended part), V_c represents the volume of the resonator, and ℓ_1 corresponds to the end correction at the flange end.

The acoustical impedance (Zr) can be expressed as follows:

$$Z_r = R_{res} + j\omega L_{res} + \frac{1}{j\omega C_{res}} \tag{8a}$$

$$L_{res} = \frac{\rho_o(L_k + \ell_1)}{SK};\ C_{res} = \frac{V_c}{\rho_o c_o^2} \tag{8b}$$

where R_{res}, L_{res}, C_{res} and ω are the acoustical resistance, acoustic inertia, acoustic compliance, and angular frequency, respectively.

According to Munjal [58], the acoustical resistance for a resonator with radius $r_r\left(=\frac{d_r}{2}\right)$ at the neck is [45]

$$\begin{aligned} R_{res} &= Y_o\left\{1 - \frac{2J_1(2k_o r_r)}{2k_o d_r}\right\} \\ &= Y_o\left\{\frac{(2k_o r_r)^2}{2\cdot 4} - \frac{(2k_o r_r)^4}{2\cdot 4^2\cdot 6} + \frac{(2k_o r_r)^6}{2\cdot 4^2\cdot 6^2\cdot 8} - \cdots\right\} \end{aligned} \tag{9}$$

where $k_o\left(=\frac{\omega}{c_o}\right)$ is the wave number and $Y_o\left(=\rho_o\frac{c_o}{SK}\right)$ is the characteristic impedance. The sound wave can be regarded as a plane wave by neglecting the high order term when $k_o r_r < 0.5$ exits.

The acoustic resistance is simplified as

$$R_{res} = Y_o\left\{\frac{(k_o r_r)^2}{2}\right\} = \frac{\rho_o \omega^2}{\pi c_o} \tag{10}$$

Therefore, the acoustical impedance (Z_r) is

$$Z_r = R_{res} + j\left[\omega L_{res} - \frac{1}{\omega C_{res}}\right] = RR + jXX \tag{11}$$

The normal sound absorbing coefficient of an extended Helmholtz resonator in Fig. 4 is

$$\alpha_{\mathrm{HR}}\left(\mathrm{f},\mathrm{d_r},\mathrm{L_k},\mathrm{V_C}\right)=1-\left|\frac{\mathrm{Z_r}-\rho_o\mathrm{c_o}}{\mathrm{Z_r}+\rho_o\mathrm{c_o}}\right| \tag{12}$$

As illustrated in Fig. 3, the sound absorbing coefficient for an extended Helmholtz type's resonator embedded within the acoustic board A can be expressed as follows:

$$\alpha_{\mathrm{HR}}\left(\mathrm{f},\mathrm{d_{r1}},\mathrm{LL_1},\mathrm{V_C}\right)=1-\left|\frac{\mathrm{Z_{r1}}-\rho_o\mathrm{c_o}}{\mathrm{Z_{r1}}+\rho_o\mathrm{c_o}}\right| \tag{13}$$

And, the equivalent averaged sound absorbing coefficient for an extended Helmholtz type's resonator is

$$\alpha_{\mathrm{HR(avg)}}\left(\mathrm{f},\mathrm{d_{r1}},\mathrm{LL_1},\mathrm{V_C}\right)=\left[\alpha_{HR}\cdot\frac{\pi d_{r1}^2}{4}\Big/L_3^2\right] \tag{14}$$

2.1.3. Overall sound absorbing Coefficient for an acoustic board A

As shown in Fig. 4-(b), associating Eq. (4) with (14), the overall averaged sound absorbing coefficient for the acoustic board A is

$$\alpha_{A(avg)}\left(RT_1,RT_2,RT_3,RT_4,RT_5,RT_6,RT_7,RT_8\right)$$

$$=\alpha_1\left(L_4^2-\frac{\pi d_{r1}^2}{4}\right)\Big/L_4^2+\alpha_{HR}\cdot\frac{\pi d_{r1}^2}{4}\Big/L_4^2 \tag{15a}$$

where $\mathrm{RT_1}=\mathrm{d_1}$; $\mathrm{RT_2}=\mathrm{pp_1}$; $\mathrm{RT_3}=\mathrm{R_1}$; $\mathrm{RT_4}=\mathrm{q_1}$; $\mathrm{RT_5}=\mathrm{Df1/Lk1}$; $\mathrm{RT_6}=\mathrm{L_2/L_o}$; $\mathrm{RT_7}=\mathrm{dr_1}$; $\mathrm{RT_8}=\mathrm{LL1/L2}$; $\mathrm{L_o}=0.3$; $\mathrm{L_{k1}}=\mathrm{q_1}+\mathrm{D_{f1}}+\mathrm{L_1}$ (15b)

2.2. Acoustic board B

2.2.1. Sound absorbing coefficients of acoustic board B's dissipative part

As illustrated in Fig. 3-(b), the acoustical board B consists of two parts: a dissipative unit (comprising two pieces of perforate plates, two layers of acoustical wools, and two layers of air gaps) and a reactive unit (consisting of one extended Helmholtz type's resonator). Similarly, the individual matrix form for the adjacent acoustical nodes within the sound absorber B's dissipative part is derived in Appendix B. As given in Appendix B, the form of the acoustic pressure p and the acoustic particle velocity u between node 3~node 4, node 4~node 5, and node 5~node 6 are given as:

$$\begin{pmatrix}p_4\\u_4\end{pmatrix}=\begin{bmatrix}cos(\omega L_2/c_o) & j\rho_o\mathrm{c_o}\sin(\omega L_2/c_o)\\ j\dfrac{\sin(\omega L_2/c_o)}{\rho_o\mathrm{c_o}} & cos(\omega L_2/c_o)\end{bmatrix}\begin{pmatrix}p_3\\u_3\end{pmatrix} \tag{16}$$

$$\begin{pmatrix}p_5\\u_5\end{pmatrix}=\begin{bmatrix}cos\left(k_{fiber2}D_{f2}\right) & jZ_{fiber2}\sin\left(k_{fiber2}D_{f2}\right)\\ j\dfrac{\sin\left(k_{fiber2}D_{f2}\right)}{Z_{fiber2}} & cos\left(k_{fiber2}D_{f2}\right)\end{bmatrix}\begin{pmatrix}p_4\\u_4\end{pmatrix} \tag{17}$$

$$\begin{pmatrix}p_6\\u_6\end{pmatrix}=\begin{bmatrix}1 & Z_{p2}\\0 & 1\end{bmatrix}\begin{pmatrix}p_5\\u_5\end{pmatrix} \tag{18}$$

The specific normal impedance at point 6 is given in Eq. (19) by developing Eq. (18)

$$Z_6=Z_5+Z_{p2} \tag{19}$$

Using the formula of the specific normal impedance and the wave number of the perforate plate from Beranek & Ver [57] yields

$$Z_{p2}=\frac{\rho_o}{pp_2}\sqrt{8\gamma\omega}\left(1+\frac{q_2}{2d_2}\right)+j\frac{\omega\rho_o}{pp_2}\left[\sqrt{\frac{8\gamma}{\omega}}\left(1+\frac{q_2}{2d_2}\right)+q_2+\delta_2\right] \tag{20a}$$

$$\delta_2=0.85(2d_2)\left(1-1.47\sqrt{pp_2}+0.47\sqrt{pp_2^3}\right) \tag{20b}$$

For normal incidence, the sound absorbing coefficient of a two-layer acouctic board (dissipative unit) [58,59] is

$$\alpha_2\left(f,pp_1,d_1,R_1,q_1,D_{f1},L_1,pp_2,d_2,R_2,q_2,D_{f2},L_2\right)$$

$$=1-\left|\frac{Z_6-\rho_o\mathrm{c_o}}{Z_6+\rho_o\mathrm{c_o}}\right|^2 \tag{21}$$

Taking into account the area percentage between the dissipative unit and the reactive unit, an equivalent average sound absorbing coefficient for each square meter of the dissipative element can be calculated as follows:

$$\alpha_{2(avg)}\begin{pmatrix} f, pp_1, d_1, R_1, q_1, D_{f1}, L_1, \\ pp_2, d_2, R_2, q_2, D_{f2}, L_2 \end{pmatrix} = \left[\alpha_2\left(L_4^2 - \frac{\pi d_{r1}^2}{4}\right) \Big/ L_4^2\right] \tag{22}$$

2.2.2. Acoustic board B's reactive part

The mechanism of the extended Helmholtz type's Resonator (HR) incorporated within the acoustic board B can be observed in Fig. 3-(b). Similarly to the derivation in section 2.1.2, the sound absorbing coefficient for the extended Helmholtz type's resonator embedded within the acoustical board B can be expressed as follows:

$$\alpha_{HR}\left(f, d_{r1}, LL_1, V_C\right) = 1 - \left|\frac{Z_{r1} - \rho_o c_o}{Z_{r1} + \rho_o c_o}\right| \tag{23}$$

And, the equivalent averaged sound absorbing coefficient for each m^2 of an extended Helmholtz type's resonator within the acoustic board B is

$$\alpha_{HR(avg)}\left(f, d_{r1}, LL_1, V_C\right) = \left[\alpha_{HR} \cdot \frac{\pi d_{r1}^2}{4} \Big/ L_4^2\right] \tag{24}$$

2.2.3. The overall sound absorbing Coefficients for an acoustic board B

Likewise, as shown in Fig. 4-(c), the overall averaged sound absorbing coefficient for the acoustic board B is

$$\alpha_{B(avg)}\left(RT_1^*, RT_2^*, RT_3^*, RT_4^*, RT_5^*, RT_6^*, RT_7^*, RT_8^*, RT_9^*, RT_{10}^*, RT_{11}^*, RT_{12}^*, RT_{13}^*, RT_{14}^*\right)$$

$$= \alpha_2\left(L_4^2 - \frac{\pi d_{r1}^2}{4}\right) \Big/ L_4^2 + \alpha_{HR} \cdot \frac{\pi d_{r1}^2}{4} \Big/ L_4^2 \tag{25a}$$

where $RT_1^* = d_1$; $RT_2^* = pp_1$; $RT_3^* = R_1$; $RT_4^* = q_1$; $RT_5^* = d_2$; $RT_6^* = pp_2$; $RT_7^* = R_2$; $RT_8^* = q_2$; $RT_9^* = L_{k2}/(L_o\text{-}L_3\text{-}L_o^*(1\text{-}RT_{12}^*))$; $RT_{10}^* = D_{f1}/L_{k1}$; $RT_{11}^* = D_{f1}/L_{k1}$; $RT_{12}^* = L_3/L_o$; $RT_{13}^* = dr_1$; $RT_{14}^* = LL_1/L_3$; $L_o = 0.3$; $L_{k1} = L_o^*(1\text{-}RT_{12}^*)^*RT_9^*$; $L_{k2} = Lo\text{-}L3\text{-}Lo^*(1\text{-}RT_{12}^*)^*RT_9^*$; $L_1 = L_{k1}\text{-}D_{f1}\text{-}q_1$; $L_2 = L_o\text{-}L_3\text{-}L_{k1}\text{-}q_2\text{-}D_{f2}$ (25b)

2.3. Sound field calculation inside a machine room

Considering a wideband noise composed of a single tone occurred inside a machine room which has dimensions of 15 m in width (W), 10 m in length (L), and 4.5 m in height (H) (as shown in Fig. 1-(a)), the acoustic board A is adopted. The acoustical pressure level ($L_{P(ijk)}$) at the j-th sound receiver emitted from the i-th machine at the k-th frequency can be expressed as follows [60,61]:

$$L_{p(ijk)}\left(L_{w(ik)}, x_i, y_i, z_i, xr_j, yr_j, zr_j, \alpha_{A-k}, L, W, H\right)$$

$$= L_{w(ik)} + 10\log\left\{\frac{Q_i}{4\pi r_{ij}^2} + \frac{4}{R_{A-k}}\right\} \tag{26a}$$

$$R_{A-k} = \frac{\sum_v^6 S_v \alpha_{A-K(v)}}{1 - \overline{\alpha}_{A-k}};\ \overline{\alpha}_k = \frac{\sum_v^6 S_v \alpha_{A-v(k)}}{\sum_v^6 S_v} \tag{26b}$$

In case of one equipment installed within the machine room, the acoustical pressure level ($L_{p(ijk)}$) at a specified receiver (xr_j, yr_j, zr_j) at the *k*-th frequency is given as

$$L_{p(ijk)} = L_{p(jk)} \tag{27}$$

The overall acoustical pressure level $L_{p(R)}$ at the receiver can be calculated by the summation of contribution from each octave band *k* ($k = 1$ to mm).

$$L_{p(RV)} = 10\log\left(\sum_{k=1}^{mm} 10^{L_{p(k)}/10}\right) \tag{28}$$

In the case of a wideband noise hybridized with a single tone using Acoustic Board B, following a similar derivation as in Case I, the acoustical pressure level ($L_{P(k)}$) at the specified receiver emitted from one machine at the k-th frequency can be expressed as [45,56,61,62]:

$$L_{p(k)}\left(L_{w(k)}, x_1, y_1, z_1, xr_1, yr_1, zr_1, \alpha_{B-k}, L, W, H\right)$$

$$= L_{w(k)} + 10\log\left\{\frac{Q_1}{4\pi r_{1,1}^2} + \frac{4}{R_{B-k}}\right\} \tag{29a}$$

$$R_{B-k} = \frac{\sum_v^6 S_v \alpha_{B-K(v)}}{1 - \overline{\alpha}_{B-k}};\ \overline{\alpha}_k = \frac{\sum_v^6 S_v \alpha_{B-v(k)}}{\sum_v^6 S_v} \tag{29b}$$

For a noisy equipment installed within the machine room, the overall acoustical pressure level ($L_{p(RV)}$) of a specified receiver RV1 (x_{r1}, y_{r1}, z_{r1}) is given as

$$L_{p(RV)} = 10\log\left(\sum_{k=1}^{mm} 10^{L_{p(k)}/10}\right) \tag{30}$$

2.4. Objective function

The assessment of the two cases with one noisy equipment inside the machine room, where the room is internally lined with two kinds of acoustical boards within a fixed thickness of 0.3 m, is discussed as follows:

2.4.1. Case I: One Noisy Equipment Installed within a Machine Room Using Acoustic Board A

The allocation of the equipment installed within a machine room, which is internally lined with acoustic board A, is illustrated in Fig. 1-(b) and 3-(a). Using the formulas of Eqs. (15) and (26), the objective function and related ranges of the parameters used in the optimization process can be obtained as

$$OBJ_1\begin{pmatrix} RT_1, RT_2, RT_3, RT_4, \\ RT_5, RT_6, RT_7, RT_8 \end{pmatrix} = L_{p(ik)} + 10\log\left\{\frac{Q_i}{4\pi r_{ij}^2} + \frac{4}{R_{A-k}}\right\} \quad (31)$$

2.4.2. Case II: One Equipment inside a Machine Room Using Acoustic Board B

Likewise, In case of one piece of equipment installed within a machine room (as shown in Fig. 1-(b) and 3-(b)), the related objective function can be obtained using the formulas provided in Eqs. (25) and (29).

$$\alpha_{B(avg)}\begin{pmatrix} RT_1^*, RT_2^*, RT_3^*, RT_4^*, RT_5^*, RT_6^*, RT_7^*, RT_8^*, \\ RT_9^*, RT_{10}^*, RT_{11}^*, RT_{12}^*, RT_{13}^*, RT_{14}^* \end{pmatrix} = L_{w(ik)} + 10\log\left\{\frac{Q_i}{4\pi r_{ij}^2} + \frac{4}{R_{B-k}}\right\} \quad (32)$$

3. Model check

Before proceeding with the optimal simulations using *APSO* (Accelerated Particle Swarm Optimization) and *SA* (Simulated Annealing) for noise attenuation in the machine room, it is essential to verify the accuracy of the acoustical absorbing coefficients for both the one-layered sound board (dissipative unit) and the extended Helmholtz resonator (reactive unit). The accuracy of the one-layered unit (consisting of the perforate front plate, acoustical wool, and air gap) presented in Eqs. (1)−(5) has been previously confirmed to be valid in a study [50]. Furthermore, the accuracy of the extended Helmholtz type resonator described in Eqs. (6)−(14) is assessed experimentally, as shown in Fig. 5. As indicated in Fig. 5, the theoretical resonating frequency for an extended Helmholtz resonator is 120 Hz which is almost the same as that of the experimental data. Therefore, the performance curve generated from the theoretical and experimental data demonstrates a high level of accuracy and agreement. This confirms the validity of the above mathematical model of acoustic board A. The model, in conjunction with the numerical method, is deemed suitable for the subsequent shape optimization in the following section.

4. Case studies

A demonstration of noise reduction in a machine room (with dimensions L = 10m, W = 15m, and H = 4.5m) housing a root blower located at coordinates (5, 3, 1) is presented in Fig. 1-(a). The original acoustical power levels ($L_{w(O)}$) for the root blower are provided in Table 1. Notably, there is a significant pure tone effect at 110 Hz with an acoustical power level of 129 dB(A). Additionally, the acoustical power levels for frequencies ranging from 63 Hz to 500 Hz exceed 100 dB(A). To mitigate the low-frequency noise together with one pure tone, two types of acoustic boards have been employed in the machine room. Case I involves acoustic board A, which consists of a single layer sound board (dissipative element) combined with one extended Helmholtz type resonator (reactive element), as depicted in Fig. 3-(a). Case II utilizes acoustic board B, which includes two layers of dissipative element along with one extended Helmholtz type resonator, as shown in Fig. 3-(b). Both types of acoustic boards are installed on the four walls and ceiling of the machine room. The thickness of the acoustic board is limited to 0.3m due to maintenance and operational requirements. To evaluate the noise levels within the machine room, an inspection station located at coordinates (5, 3, 1) is used to calculate the resulting acoustical pressure level, denoted as $L_{p(RV1)}$. Numerical assessments employing *APSO* and *SA* optimizers are adopted for optimal acoustical performance within the limited space.

5. Sensitivity analysis

Before proceeding with the optimization of noise abatement in the machine room, a sensitivity analysis of the sound absorbing coefficient at the receiver with respect to the geometric parameters of acoustic board A is conducted. Using Eq. (15) (26), the impact of the sound absorbing coefficient at the receiver under various design parameters and frequencies is illustrated in Fig. 6-(a)~(f) and 7(a)~(c). Fig. 6-(a) shows that the sound absorbing coefficient

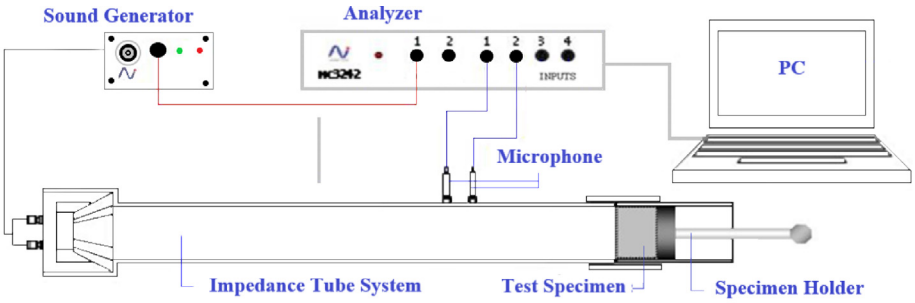

(a) Experimental instrument

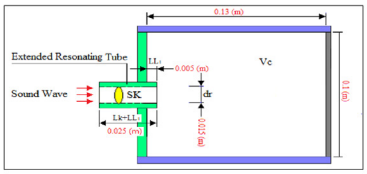

(b) Specimen

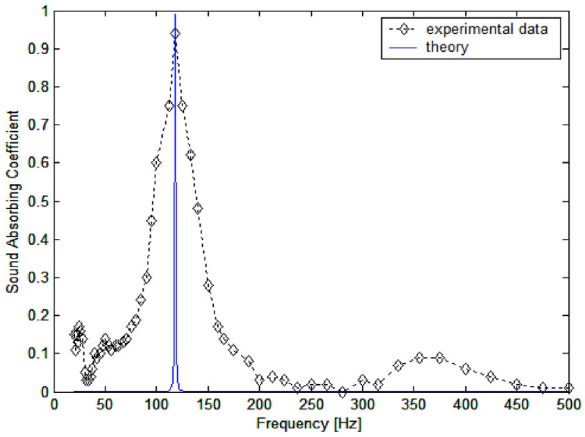

(c) Comparison of theoretical sound absorbing coefficient and experimental data.

Fig. 5. Experiment Facility and comparison for an extended Helmholtz resonator.

at the receiver increases with an increase in q_1 (the depth of the perforate plate's holes). Conversely, Fig. 6-(b) indicates that the sound absorbing coefficient decreases as d_1 (the diameter of the perforated front plate's holes) increases. Additionally, the sound absorbing coefficient exhibits higher values at higher frequencies due to the acoustical effects of the dissipative part. Fig. 6-(c) demonstrates that the absorption coefficient significantly increases with an increase in pp_1 (porosity of the perforate front plate). Similarly, Fig. 6-(d) shows that the absorption coefficient exhibits a substantial increase when D_{f1} (depth of the acoustical wool) increases. Furthermore, Fig. 6-(e) indicates a slight increase in the absorption coefficient with an increase in R_1 (flow resistance of the acoustical wool). As shown in Fig. 6-(f), the acoustical absorption coefficient increases, and the tuned frequency shifts to a higher frequency range as L_1 (air gap of the one-layered acoustical board's dissipative part) increases. This is because the depth of the resonator decreases with an increase in L_1 with a fixed thickness of the acoustical board. Consequently, the resonating frequency increases, leading to an increase in the sound absorption coefficient of the one-layered sound board at lower frequencies due to the increased air gap. In addition to the dissipative part, the reactive part of the acoustical board also plays a role.

It is observed in Fig. 7-(a) that there is no change in the sound absorbing coefficient at the receiver when d_{r1} (the resonating tube's diameter) increases.

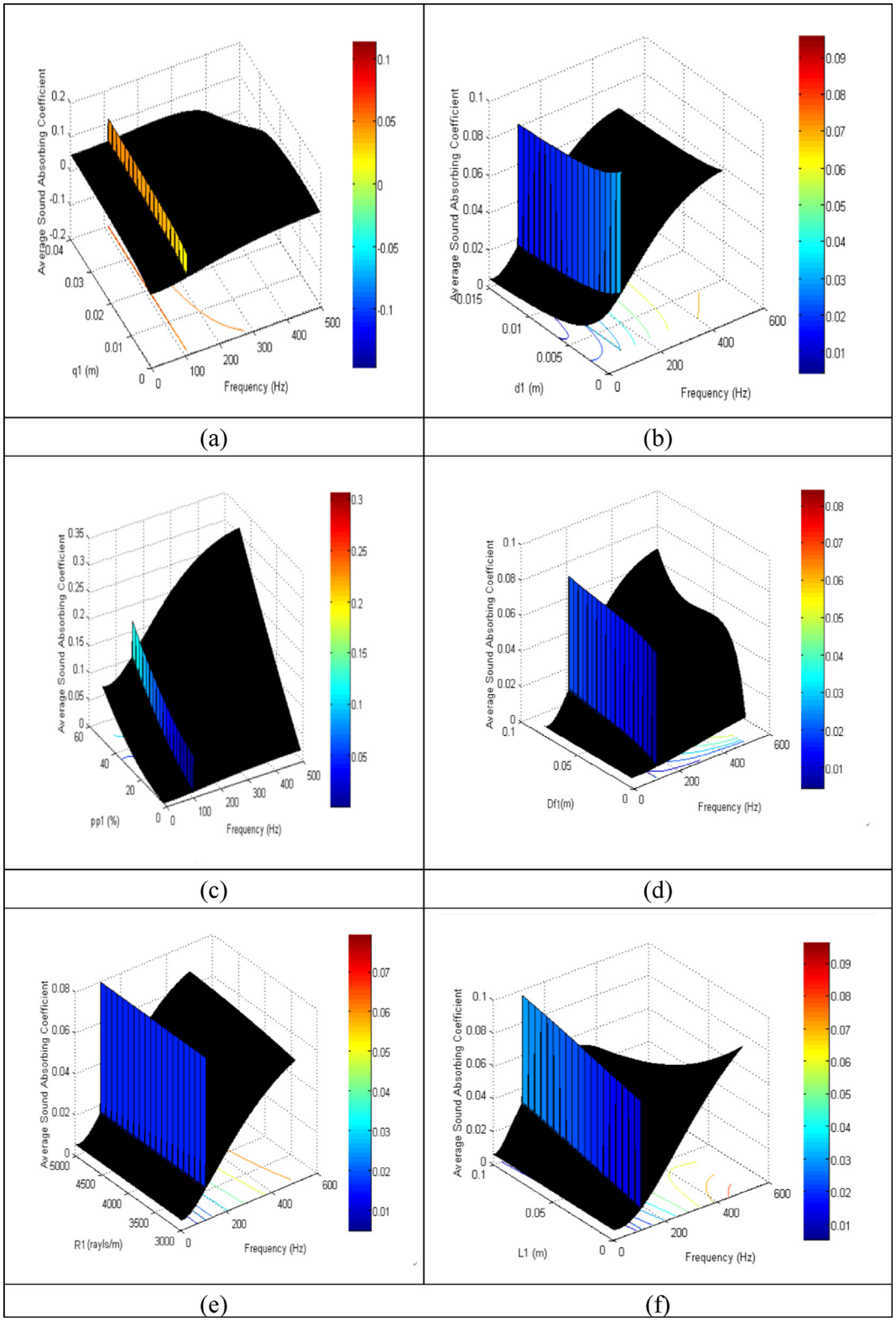

Fig. 6. Relationship of sound absorbing coefficient to (a) q_1 and frequency f, (b) d_1, and frequency f (c) pp_1 and frequency f, (d) D_{f1} and frequency f, (e) R_1 and frequency f, (f) L_1 and frequency f (one-layer sound board within the acoustic board A).

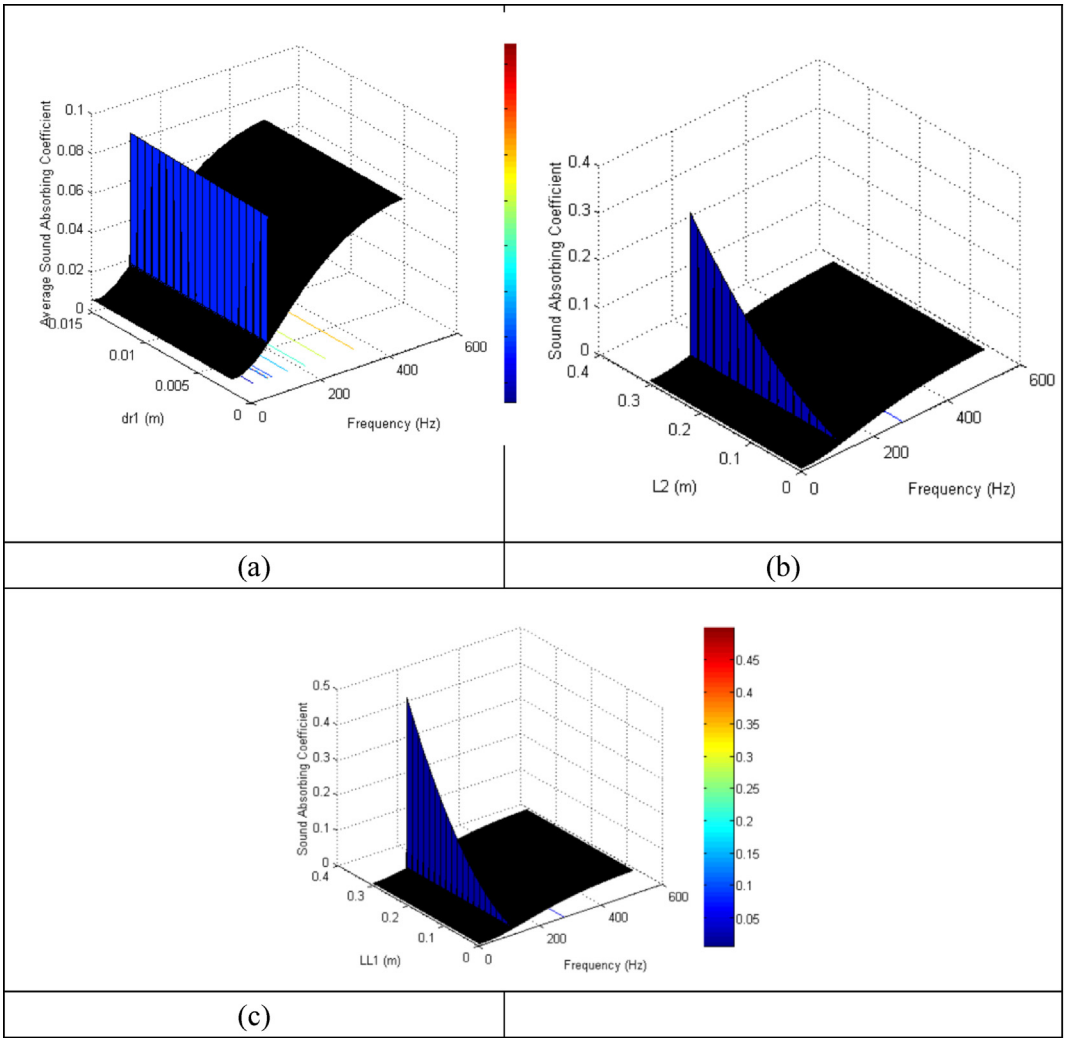

Fig. 7. Relationship of sound absorbing coefficient to (a) d_{r1} and frequency f, (b) L_2, and frequency f (c) LL_1 and frequency f (one-chamber extended tube of the Helmholtz resonator within the acoustical board A).

However, in Fig. 7-(b), the absorption coefficient of the resonator increases with an increase in L_2 (depth of the resonator). Similarly, in Fig. 7-(c), the absorption coefficient of the resonator increases with an increase in LL_1 (internally extended length of a resonating tube). For acoustic board B, the impact of the sound absorbing coefficient at the receiver under various design parameters and frequencies is illustrated in Fig. 8-(a)~(f), Fig. 9-(a)~(f), and Fig. 10(a)~(c) using Eq. (25) (29). Figs. 8-(a)~(f) and Fig. 9-(a)~(f) demonstrate that changes in the geometric parameters (q1, q2, d1, d2, pp1, pp2, Df1, Df2, R1, R2) of the first and second layers can affect the sound absorbing coefficient of acoustic board B. Furthermore, profiles in Fig. 8-(f) and Fig. 9-(f) reveal that the sound absorbing coefficient can be manipulated by changing the air gaps L_1 and L_2. Regarding the reactive part, Fig. 10-(a) shows that the resonating frequency shifts to a higher frequency range as the d_{r1} (diameter of the resonating tube) increases. Conversely, Fig. 10-(b) indicates that the resonating frequency shifts to a lower frequency range when the L3 (depth of the resonating chamber) increases. Fig. 10-(c) suggests that the sound absorbing coefficient exhibits minimal change as the LL1 (internally extended length of the resonating tube) varies.

As analyzed above, the geometric parameters of the acoustical boards and resonator play an essential role in the design of the sound absorbing coefficient and significantly impact the acoustical field inside the machine room. Consequently, all the geometric parameters of acoustic boards A and B are considered as design parameters during the minimization of the acoustical pressure level at the receiver (RV_1). These parameters are optimized for desired acoustical performance and noise reduction in the machine room.

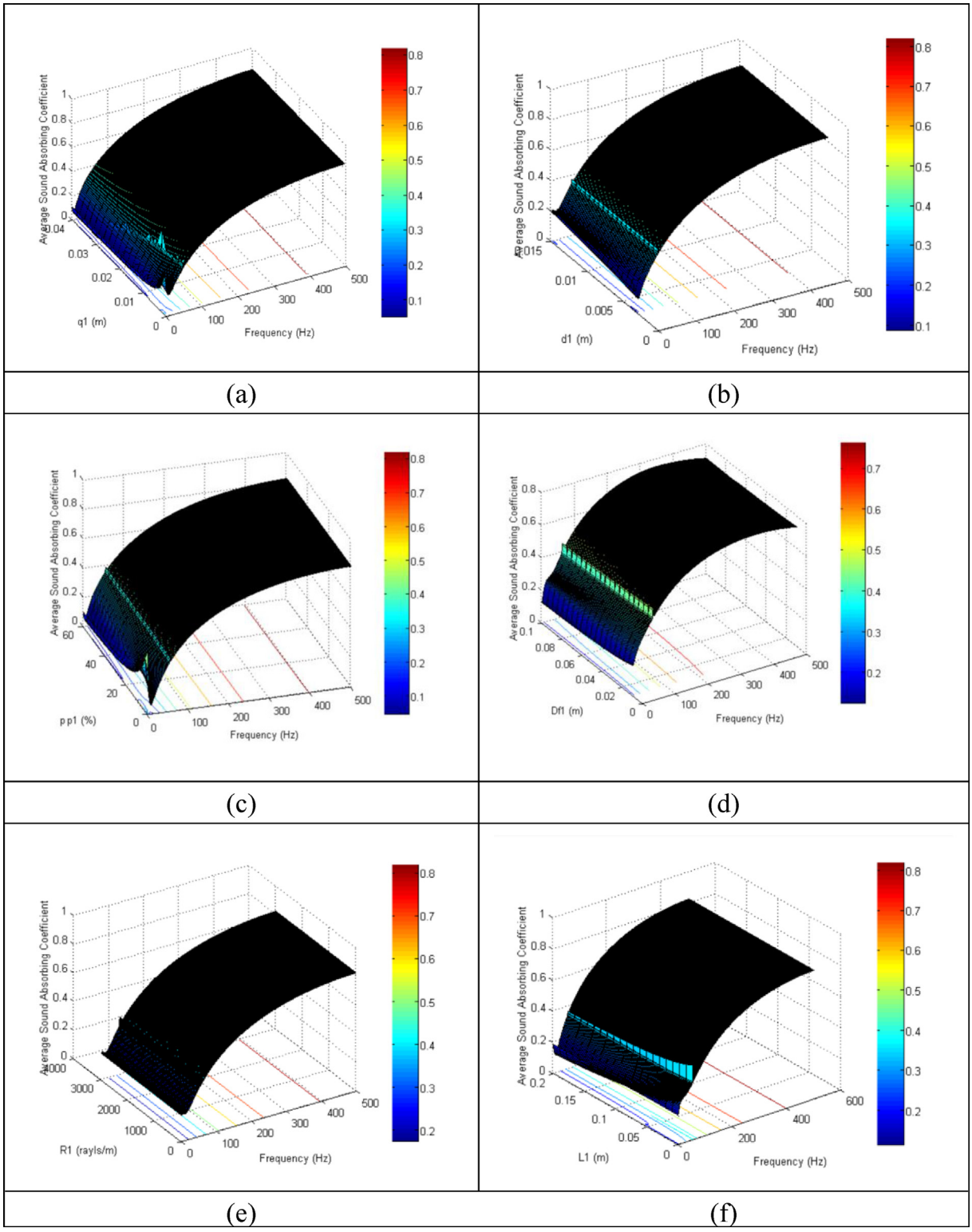

Fig. 8. Relationship of sound absorbing coefficient to (a) q_1 and frequency f, (b) d_1, and frequency f (c) pp_1 and frequency f, (d) D_{f1} and frequency f, (e) R_1 and frequency f, (f) L_1 and frequency f (first layer sound board within the acoustical board B).

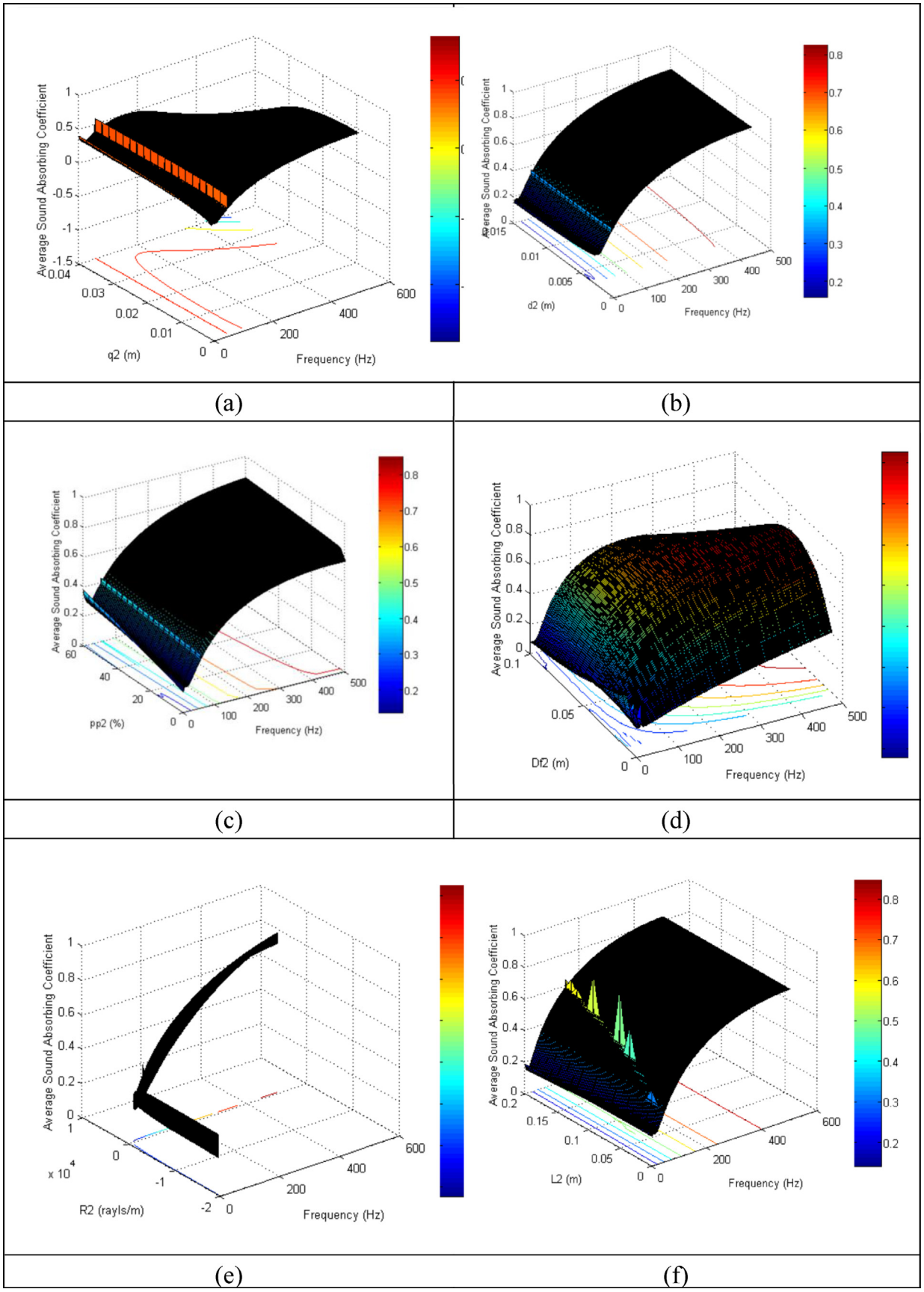

Fig. 9. Relationship of sound absorbing coefficient to (a) q_2 and frequency f, (b) d_2, and frequency f (c) pp_2 and frequency f, (d) D_{f2} and frequency f, (e) R_2 and frequency f, (f) L_2 and frequency f (second layer sound board within the acoustical board B).

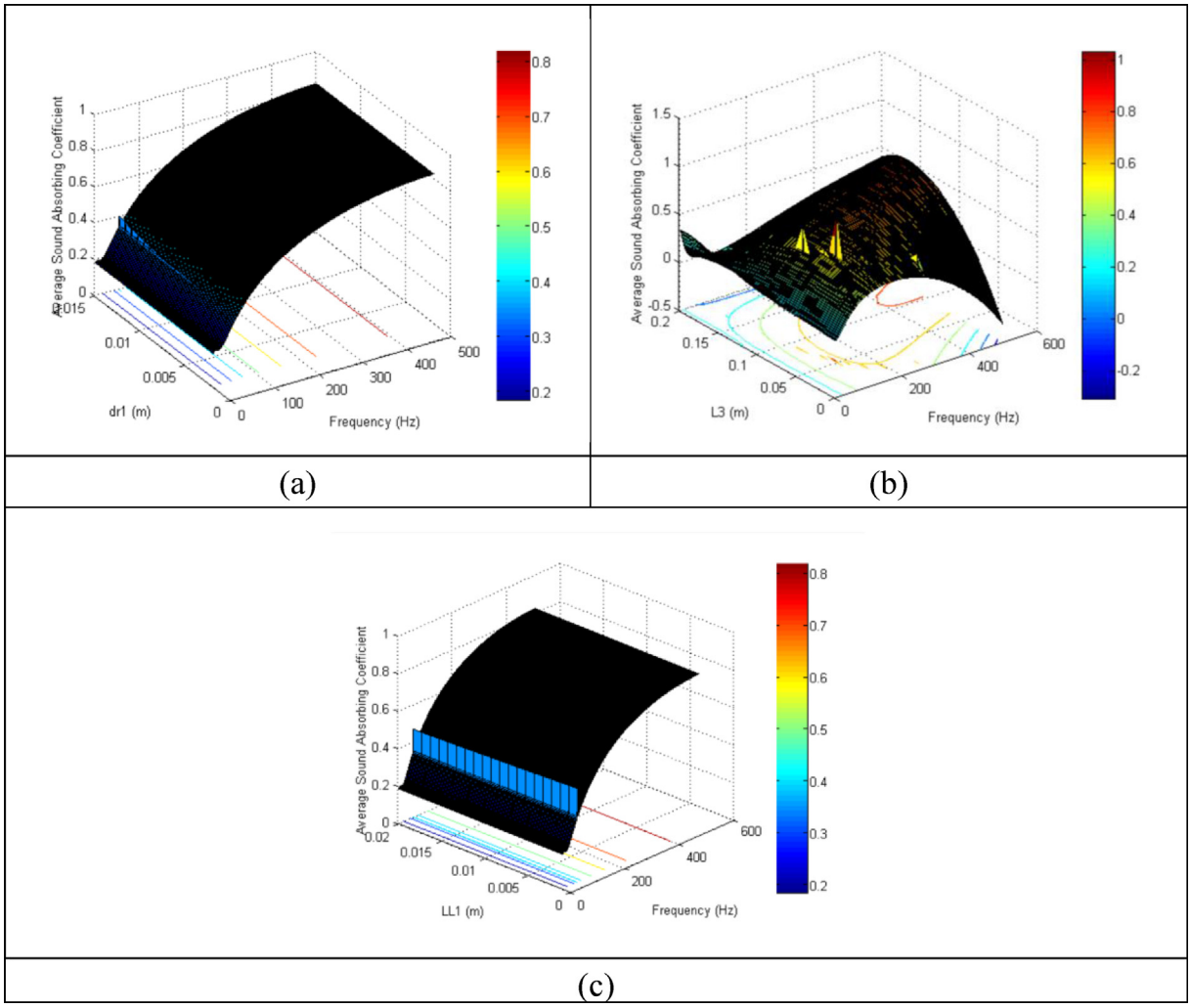

Fig. 10. Relationship of sound absorbing coefficient to (a) d_{r1} and frequency f, (b) L_3, and frequency f (c) LL_1 and frequency f (one-chamber extended tube of the Helmholtz resonator within the acoustical board B).

6. Optimization

6.1. Particle swarm optimization

Particle Swarm Optimization (*PSO*) is an evolutionary computing technique developed by Kenney and Eberhart in 1995 [63−65], and seen in widespread applications, including optimization, computational intelligence, and design/scheduling [45,55,56]. Inspired by fish schools and bird flocks, *PSO* operates by initializing a random population of particles or individuals. The movement of each particle is governed by two major components: a stochastic component and a deterministic component. The particles are attracted towards the position of the current global best solution G^{best} as well as their own best-known position x_i^{best}. This collective behavior guides the particles towards better solutions. In *PSO*, each particle has a position vector x_i and a velocity vector v_i. The new velocity vector is determined using the following formula, combining both the individual and global best positions:

$$v_i^{t+1} = v_i^t + \alpha\epsilon_1\left|g^* - x_i^t\right| + -\beta\epsilon_2\left|x_i^{best} - x_i^t\right| \tag{33}$$

where ϵ_1 and ϵ_2 are two random vectors, both with a value between 0 and 1.

The *PSO* algorithm typically utilizes both the current global best solution G^{best} and the individual best solution x_i^{best} to guide the particles' movement. However, it has been observed that the inclusion of individual best information does not always provide significant benefits [66]. Therefore, a simplified version of *APSO* (Accelerated Particle Swarm Optimization), known as the global best-only *APSO*, has been proposed [67,68]. This variant relies solely on the global best solution to accelerate the convergence of the algorithm.

$$v_i^{t+1} = v_i^t + \alpha\epsilon_n + \beta\left(\mathrm{G}^{\mathrm{best}} - x_i^t\right) \quad (34)$$

where ϵ_n is a random number between 0 and 1. The update of the position is expressed as

$$x_i^{t+1} = x_i^t + v_i^{t+1} \quad (35)$$

Generally, it is sufficient for most applications with $\alpha = 0.1 \sim 0.5$ and $\beta = 0.1 \sim 0.7$ [66]. The number of particles in the *APSO* algorithm also plays a role in the convergence of its iterations. The termination criterion for the *APSO* algorithm typically includes a maximum number of iterations ($\mathrm{iter}_{\max}$). The flow diagram of the *APSO* process is illustrated in Fig. 11.

6.2. Simulated annealing method [48, 52, 53, 54]

Simulated Annealing (*SA*) is an optimization technique that originated from physical metallurgy. It was first introduced by Metropolis et al. [69] and further developed by Kirkpatrick et al. [70]. The *SA* algorithm draws inspiration from the slow cooling process in metallurgy, where a material is cooled gradually to maintain its state close to the minimal energy configuration for a more uniform crystalline structure. In the *SA* process, an initial solution is randomly selected to start the optimization. The algorithm aims to explore the solution space and converge towards an optimal solution by iteratively modifying the current solution. The process is illustrated in Fig. 12. For each iteration, a new random solution (X') is generated from the neighborhood of the current solution (X). The neighborhood is typically defined by some predefined search operators or perturbation methods. The objective function (or system energy) is then evaluated for both the current solution (X) and the new solution (X'). If the difference in the objective function

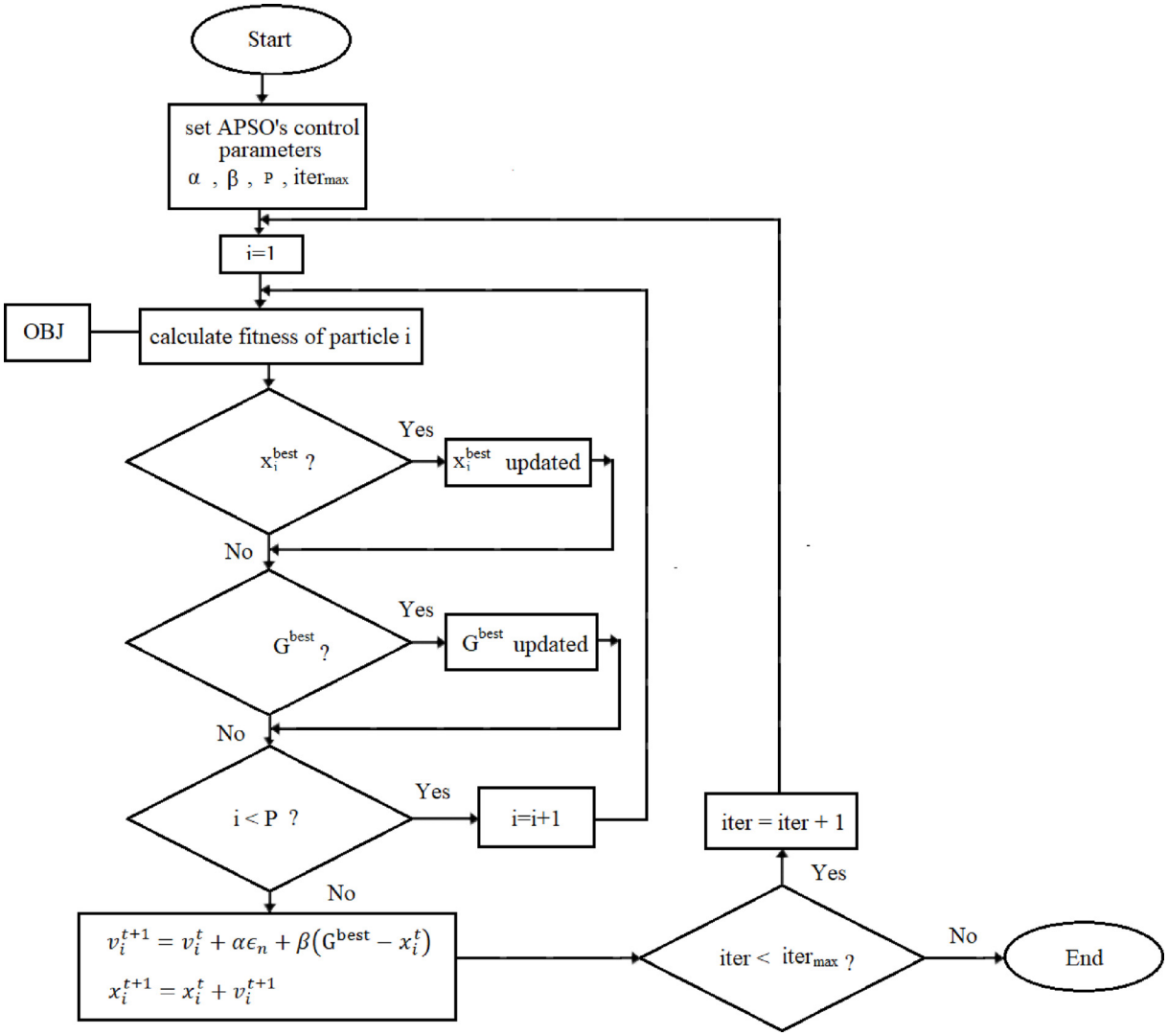

Fig. 11. A flow diagram of APSO algorithm.

($\Delta E = E(X') - E(X)$) is negative ($\Delta E < 0$), indicating an improvement in the solution quality, the new solution is accepted with a transition probability ($pb(X')$) of 1. In other words, the new solution is always considered better and immediately adopted as the current solution. However, if the difference in the objective function is positive ($\Delta E > 0$), indicating a potential deterioration in the solution quality, the algorithm employs a probabilistic approach to determine whether to accept the new solution or not. The transition probability ($pb(X')$) is evaluated using the Boltzmann's factor, which considers the temperature parameter (T) and the magnitude of ΔE. The transition probability is calculated as $pb(X') = \exp(-\Delta E/T)$.

$$pb(X') = \begin{cases} 1, \Delta F \le 0 \\ \exp\left(\frac{-\Delta F}{CT}\right), \Delta F > 0 \end{cases} \tag{36a}$$

$$\Delta F = F(X') - F(X) \tag{36b}$$

If the transition probability (pb (X')) is greater than a randomly generated value between 0 and 1, it signifies that the algorithm is willing to accept a new solution even if it leads to a higher energy condition. Conversely, the new solution will be discarded if the transition probability is lower than the randomly generated value. This process of perturbing the current solution and evaluating the change in the objective function continues until the maximum number of iterations ($iter_{max}$) is reached. During the *SA* process (as shown in Fig. 13), as the iteration progresses, successful substitutions of the current solution are made, allowing the algorithm to explore the solution space. For each iteration, the temperature gradually decreases, affecting the acceptance probability of worse solutions. This temperature decay is achieved using a cooling schedule, which controls the rate at which the temperature decreases.

$$T_{new} = kk * Told \tag{37}$$

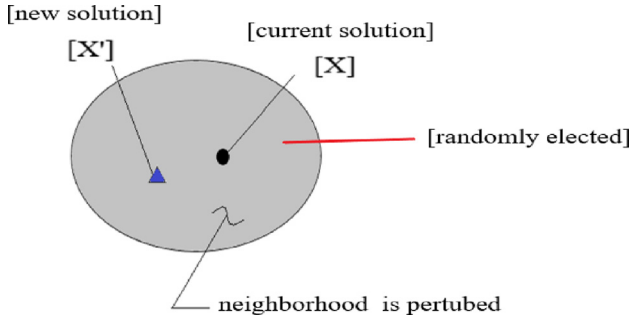

Fig. 12. Solution select scheme in SA.

Looking at Case I, the optimization of geometric design parameters for acoustic board A was achieved by utilizing Eq. (31) in conjunction with both the *APSO* and *SA* algorithms, considering the space-constrained condition. The *APSO* and *SA* algorithms were used to explore the solution space and search for the optimal values of the design parameters. By iteratively updating the positions of particles in the *APSO* algorithm and performing simulated annealing steps in the *SA* algorithm, the optimization process aimed to minimize the objective function defined by Eq. (31) while satisfying the space constraints. Similarly, in Case II, the optimization of geometric design parameters for acoustic board B was obtained using Eq. (32) in conjunction with the *APSO* and *SA* algorithms under the space-constrained condition. The *APSO* and *SA* algorithms were applied to search for the optimal values of the design parameters that minimized the objective function defined by Eq. (32). By iteratively updating the particle positions in *APSO* and performing simulated annealing steps in *SA*, the algorithms aimed to find the optimal configuration of geometric parameters for acoustic board B, considering the space constraints.

7. Results and discussion

7.1. Results

Various *APSO* parameters were considered to achieve effective optimization, including inertial weight factors (α, β), particle population size (p), and

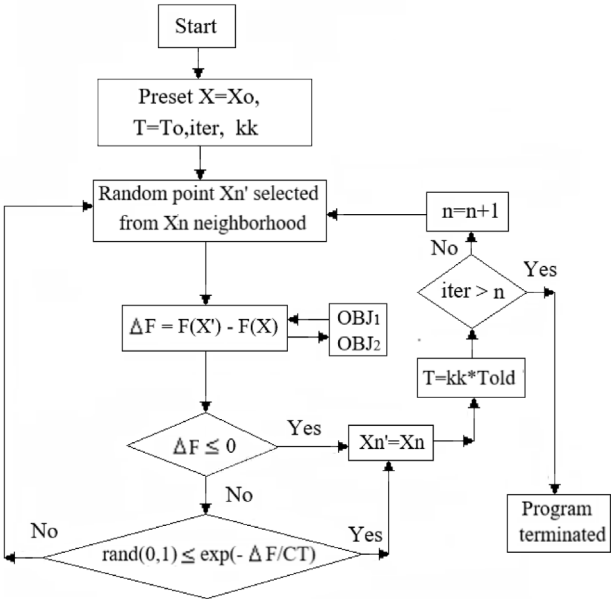

Fig. 13. Block diagram of the SA process.

the maximum number of iterations ($iter_{max}$). The following ranges were explored for these parameters: α =(0.5, 0.6, 0.7, 0.8, 0.9, 1.0);β =(0.1, 0.2, 0.3, 0.4, 0.5, 0.6, 0.7); p = (20, 30, 40, 50, 60, 70); and, $iter_{max}$ =(50, 100, 500, 1000, 2000, 5000). By varying these parameters, the optimization process explored different combinations to find the optimal solutions for Case I and Case II. The results of the two optimizations are presented below.

7.1.1. Case I

The distribution of acoustical pressure level (L_p) at a height of 1.0 m in the machine room, prior to adding acoustic board A, is illustrated in Fig. 14-(a). To minimize the acoustical pressure level at the receiver (RV1) using Eq. (31) and the predefined range of design parameters shown in Table 2, an optimization process was conducted. The results of this optimization, considering various *APSO* control parameter sets, are presented in Table 3. Table 3 showcases the outcomes obtained from trying twenty-two sets of *APSO* parameters during the optimization. Notably, the set of *APSO* control parameters (α, β, p, $iter_{max}$) = (0.6, 0.5, 30, 5000) yielded the nearly optimal design data, with the lowest acoustical pressure level ($L_{p(RV1)}$) of 118.157 dB(A) at the receiver, as indicated in the last entry of Table 3.

Similarly, by utilizing Eq. (31) in combination with the *SA* optimizer, the optimal design of acoustic board A was obtained, resulting in the lowest acoustical pressure level ($L_{p(RV1)}$) of 118.199 dB(A) at the receiver. The optimized design data is presented in Table 4. A comparison between the optimal design data obtained from the *APSO* method and the *SA* method, as displayed in Table 4, reveals that the *APSO* method achieved slightly better acoustical results compared to the *SA* method.

Fig. 14-(b) presents the distribution curves of the acoustical pressure level (L_p) at a height of 1.0 m in the machine room by applying the optimal design

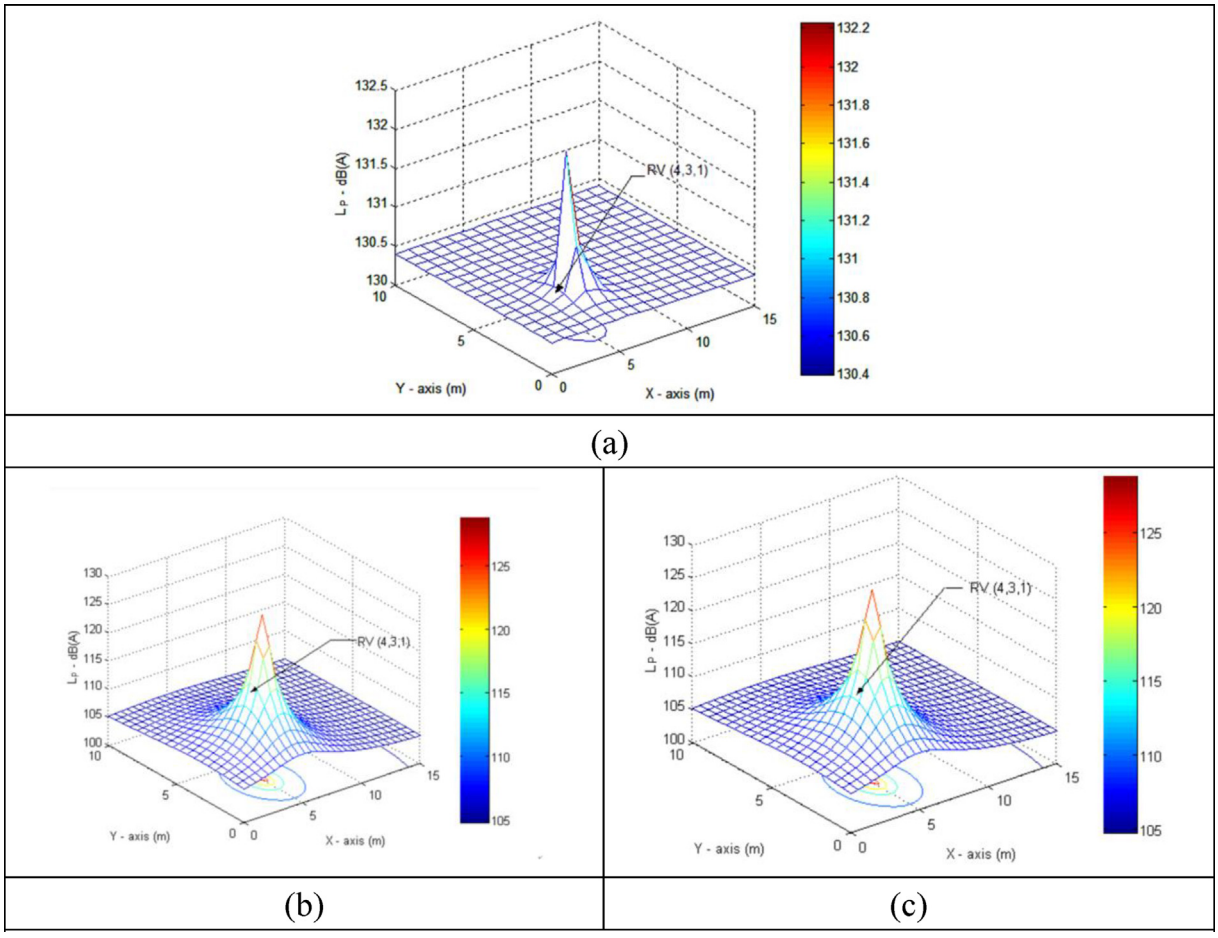

Fig. 14. Noise contour map (Lp at height of 1 m) of a machine room (a) without adding the acoustical boards A and B (b) adding the acoustical board A, (c) adding the acoustical board B.

Table 2. Parameter range of an one-layer sound board hybridized with an extended Helmholtz resonator. (acoustic board A).

Design parameters							
RT_1 (m)	RT_2	RT_3 (rayls/m)	RT_4 (m)	RT_5	RT_6	RT_7 (m)	RT_8
[0.003, 0.015]	[0.05, 0.3]	[3000, 20,000]	[0.001, 0.003]	[0.3, 0.7]	[0, 0.05]	[0.005, 0.147]	[0.2, 0.8]

Note: $RT_{1=}d_1$; $RT_2 = pp_1$; $RT_3 = R_1$; $RT_4 = q_1$; $RT_5 = D_{f1}/L_{k1}$; $RT_6 = L_2/L_o$; $RT_7 = dr_1$; $RT_8 = LL_1/L_2$;$L_o = 0.3$; $L_{k1} = q1+D_{f1}+L_1$.

Table 3. Optimal acoustical pressure level of a receiver (RV1) using a one extended HR and one-layer sound board at various APSO parameters (Case I: acoustic board A).

Item	*APSO* parameters				Design parameters								$OBJ_1 - Lp_{(RT)}$ -dB(A)
	α	β	p	$iter_{max}$	RT_1 (m)	RT_2	RT_3 (rayls/m)	RT_4 (m)	RT_5	RT_6	RT_7 (m)	RT_8	
1	0.5	0.1	40	50	0.0033	23.2	15,482	0.0030	0.402	0.497	0.012	0.722	118.1766
2	0.6	0.1	40	50	0.0031	26.7	9856	0.0026	0.337	0.593	0.014	0.350	118.1638
3	0.7	0.1	40	50	0.0054	24.0	11,424	0.0019	0.309	0.334	0.006	0.591	118.1706
4	0.8	0.1	40	50	0.0030	21.5	14,750	0.0026	0.398	0.490	0.014	0.577	118.1781
5	0.9	0.1	40	50	0.0038	25.0	7086	0.0026	0.524	0.441	0.004	0.577	118.1772
6	1.0	0.1	40	50	0.0036	19.6	11,520	0.0027	0.313	0.313	0.012	0.340	118.1658
7	0.6	0.2	40	50	0.0033	16.9	12,057	0.003	0.316	0.368	0.002	0.530	118.1803
8	0.6	0.3	40	50	0.0030	24.3	12,074	0.003	0.318	0.326	0.011	0.616	118.1607
9	0.6	0.4	40	50	0.0030	24.4	9425	0.003	0.326	0.301	0.007	0.702	118.1601
10	0.6	0.5	40	50	0.003	26.0	13,346	0.003	0.305	0.320	0.007	0.458	118.1596
11	0.6	0.6	40	50	0.003	25.1	13,273	0.003	0.300	0.322	0.003	0.238	118.1599
12	0.6	0.7	40	50	0.003	22.7	4730	0.003	0.300	0.300	0.013	0.360	118.1608
13	0.6	0.5	20	50	0.003	22.2	10,238	0.003	0.509	0.487	0.010	0.750	118.1764
14	0.6	0.5	30	50	0.003	28.9	13,455	0.003	0.31′0	0.325	0.005	0.750	118.1583
15	0.6	0.5	50	50	0.003	19.1	10,456	0.003	0.304	0.319	0.009	0.477	118.1633
16	0.6	0.5	60	50	0.003	19.1	10,574	0.003	0.339	0.326	0.004	0.679	118.1648
17	0.6	0.5	70	50	0.003	24.7	12,583	0.003	0.302	0.331	0.007	0.436	118.1601
18	0.6	0.5	30	100	0.003	23.3	12,356	0.003	0.300	0.308	0.015	0.309	118.1607
19	0.6	0.5	30	500	0.003	27.4	14,716	0.003	0.3	0.327	0.014	0.725	118.1590
20	0.6	0.5	30	1000	0.003	22.5	13,196	0.003	0.3	0.320	0.010	0.226	118.1614
21	0.6	0.5	30	2000	0.003	28.2	14,530	0.003	0.3	0.326	0.010	0.373	118.1586
22	0.6	0.5	30	5000	0.003	30.0	10,266	0.003	0.3	0.3	0.010	0.434	118.157

data in a theoretical calculation, after incorporating the acoustic board A. Additionally, the average sound absorbing coefficient (α) for the optimal acoustic board A is calculated and depicted in Fig. 15. Furthermore, a comparison of the $L_{p(RV1)}$ spectrum at the receiver, both before and after the integration of the acoustic board A, is illustrated in Fig. 16.

7.1.2. Case II

Eq. (32), along with the specified range of design parameters from Table 5, was utilized for the optimization of acoustic board B. The minimization of the acoustical pressure level ($L_{p(RV1)}$) at the receiver (RV1) was performed using various *APSO* control parameter sets, and the results are presented in Table 6. It is observed from Table 6 that the $L_{p(RV1)}$ at the receiver is minimized to 118.144 dB(A) when the *APSO* control parameters are set to (α, β, p, $iter_{max}$) = (0.6, 0.5, 30, 5000). Similarly, employing Eq. (32) in conjunction with the *SA* optimizer, the optimal design of acoustic board B achieves a receiver's lowest $L_{p(RV1)}$ of 118.267 dB(A) as shown in Table 6. A comparison between the $L_{p(RV1)}$ results obtained from *APSO* and *SA* methods indicates that the *APSO* method yields a slightly better acoustic effect.

The resulting curves depicting the distribution of L_p at a 1.0 m above the ground inside the machine room after integrating the acoustic board B is obtained by utilizing the better design data and theoretical formula and shown in Fig. 14-(c). Additionally, the total sound absorbing coefficient (α) for the

Table 4. Comparison of optimal acoustical pressure level (at a receiver RV1) for a one-layer sound board (equipped with an extended HR) Between the APSO method and the SA method (Case I: acoustic board A).

Item	Design parameters								$OBJ_1 - Lp_{(RT)}$ -dB(A)
	RT_1 (m)	RT_2	RT_3 (rayls/m)	RT_4 (m)	RT_5	RT_6	RT_7 (m)	RT_8	
APSO	0.0033	30.0	10,266	0.003	0.3	0.3	0.010	0.434	118.1570
SA	0.0090	27.5	16,968	0.002	0.627	0.564	0.006	0.374	118.1988

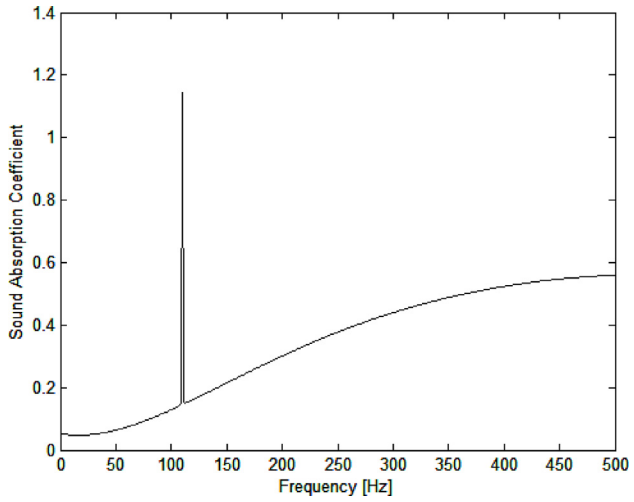

Fig. 15. Sound absorbing coefficient of an optimized one-layer sound board hybridized with an extend Helmholtz resonator (acoustical board A).

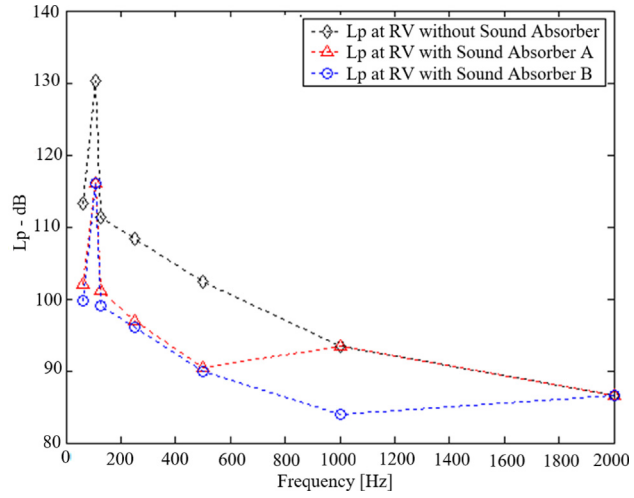

Fig. 16. Spectrum of acoustical pressure level (L_p) at the receiver RV1 before and after the optimal one-layer sound board hybridized with one extended Helmholtz resonator is added (acoustical board A).

optimized acoustic board B was evaluated and depicted in Fig. 17. Furthermore, Fig. 16 illustrates the comparison of $L_{p(RV1)}$ spectra at the receiver before and after integrating the acoustic board B. To differentiate the sound attenuations between acoustic boards A and B, a comparison of their sound attenuations is plotted in Fig. 18. It is observed from Fig. 18 that the sound attenuation of acoustic board B is broader compared to that of acoustic board A. As a result, the optimal geometric data for acoustic board A and acoustic board B have been calculated and presented in Tables 7 and 8, respectively.

7.2. Discussion

The distribution of L_p in Fig. 14-(a) and Fig. 14-(b) shows clearly that the acoustical pressure profile in Fig. 14-(a) is relatively uniform compared to that in Fig. 14-(b). This observation indicates that the acoustic board A efficiently reduces the reverberation component, leaving only the direct part of the sound energy. Additionally, Fig. 15 illustrates the precise tuning of the overall averaged sound absorbing coefficient (α) of the acoustical board A to the tone of 110 Hz. Furthermore, From Fig. 16, it demonstrates an improvement of 15 dB in the $L_{p(RV1)}$ at the receiver when adding the acoustic board A. Similarly, the profile of Fig. 14-(a) appears flatter than that of Fig. 14-(c), implying an effective reduction of the reverberation component when using the acoustic board B. Furthermore, Fig. 17 highlights the precise tuning of the averaged sound absorption coefficient (α) of the acoustic board B at the tone of 110 Hz. Moreover, as indicated in Fig. 16, the $L_{p(RV1)}$ at the receiver is eliminated by 15 dB with the acoustic board B incorporated. Moreover, as illustrated in Fig. 18, the acoustical attenuation of the acoustic board B is broader compared to that of the acoustic board A. Consequently, the overall noise abatement performance in Case II is superior to that of Case I.

Table 5. Parameter range of a two-layer sound board hybridized with an extended Helmholtz resonator. (acoustic board B).

Design parameters							
RT_1* (m)	RT_2*	RT_3* (rayls/m)	RT_4* (m)	RT_5* (m)	RT_6*	RT_7* (rayls/m)	RT_8* (m)
[0.003, 0.015]	[0.05, 0.3]	[3000, 20,000]	[0.001, 0.003]	[0.003, 0.015]	[0.05, 0.3]	[3000, 20,000]	[0.001, 0.003]
RT_9*	RT_{10}*	RT_{11}*	RT_{12}*	RT_{13}* (m)	RT_{14}*		
[0.3, 0.7]	[0.3, 0.7]	[0.3, 0.7]	[0.3, 0.7]	[0.002, 0.015]	[0.2, 0.8]		

Note: RT_1*=d_1; RT_2* = pp_1; RT_3* = R_1; RT_4* = q_1; RT_5*=d_2; RT_6* = pp_2; RT_7* = R_2; RT_8* = q_2; RT_9* = $L_{k2}/(L_o\text{-}L_3\text{-}L_o*(1\text{-}\ RT_{12}*))$; RT_{10}* = D_{f1}/L_{k1}; RT_{11}* = D_{f1}/L_{k1};RT_{12}* = L_3/L_o; RT_{13}* = dr_1; RT_{14}* = LL_1/L_3;L_o = 0.3; L_{k1} = L_o*(1- RT_{12}*)* RT_9*; L_{k2} = Lo-L3-Lo*(1-RT_{12}*)* RT_9*; L_1 = L_{k1}-D_{f1}-q_1; L_2 = L_o-L_3-L_{k1}-q_2-D_{f2}.

Table 6. Optimal acoustical pressure level of a receiver RV1 using an one extended HR and two-layer sound board (Case II: acoustic board B).

item	Design parameters								OBJ_2 − $Lp_{(T)}$ -dB(A)
APSO	RT_1* (m)	RT_2*	RT_3* (rayls/m)	RT_4* (m)	RT_5* (m)	RT_6*	RT_7* (rayls/m)	RT_8* (m)	118.1440
	0.0134	24.7	16,940	0.00280	0.0147	19.6	19,077	0.0024	
	RT_9*	RT_{10}*	RT_{11}*	RT_{12}*	RT_{13}* (m)	RT_{14}*			
	0.375	0.451	0.631	0.390	0.010	0.730			
SA	RT_1* (m)	RT_2*	RT_3* (rayls/m)	RT_4* (m)	RT_5* (m)	RT_6*	RT_7* (rayls/m)	RT_8* (m)	118.2670
	0.0053	16.1	3220	0.00162	0.0135	25.9	8663	0.0028	
	RT_9*	RT_{10}*	RT_{11}*	RT_{12}*	RT_{13}* (m)	RT_{14}*			
	0.492	0.524	0.546	0.565	0.010	0.611			

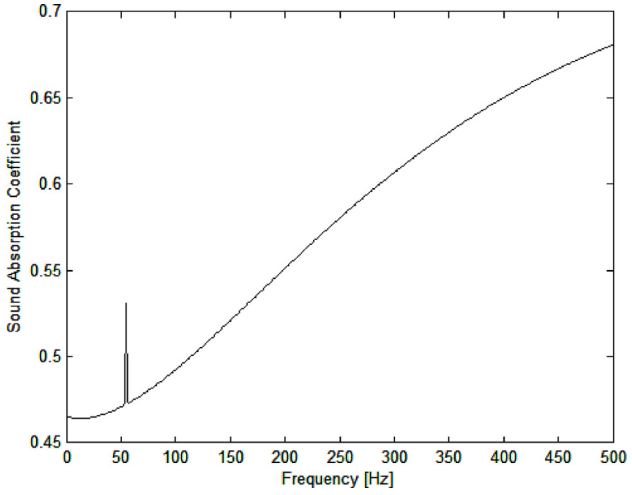

Fig. 17. Sound absorbing coefficient of an optimized two-layer sound board hybridized with an extend Helmholtz resonator (acoustical board B).

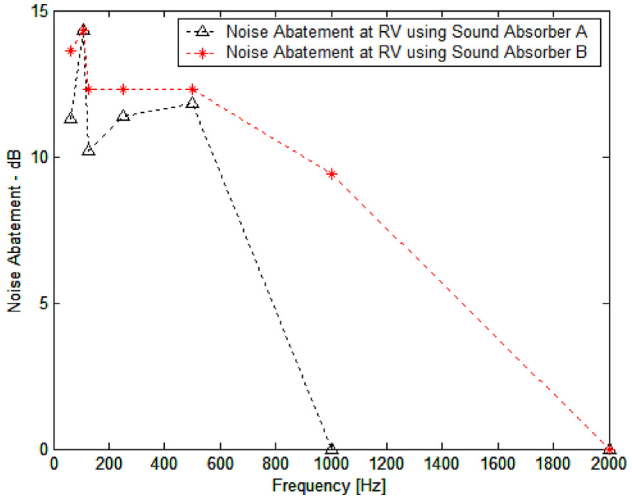

Fig. 18. Spectrum of acoustical pressure level $Lp_{(RV1)}$ at the receiver before and after the optimal two-layer sound board hybridized with one extended Helmholtz resonator is added (acoustical board B).

Table 7. Optimal dimension for an one extended HR and one-layer sound board (Case I: acoustic board A).

d_1 (m)	pp_1	R_1 (rayls/m)	q_1 (m)	L_2 (m)	dr_1 (m)	LL_1 (m)	D_{f1} x(m)
0.003	0.30	10265.6	0.003	0.009	0.0102	0.039	0.063

Table 8. Optimal dimension for an one extended HR and two-layer sound board (Case II: acoustic board B).

d_1 (m)	pp_1	R_1 (rayls/m)	q_1 (m)	d_2 (m)	pp2	R_2 (rayls/mm)	q_2 (m)
0.0135	0.247	16940.2	0.003	0.015	0.196	19077.2	0.002
L_1 (m)	D_{f1} (m)	L_3 (m)	L_2 (m)	D_{f2} (m)	d_{r1} (m)	LL_1 (m)	
0.035	0.031	0.117	0.004	0.064	0.010	0.730	

8. Conclusion

The study highlights the significant influence of geometric parameters on the sound absorbing coefficient of acoustic boards A and B. To efficiently reduce reverberant sound energy, two types of acoustic boards were utilized: acoustic board A, consisting of a single layer of dissipative element and a modified Helmholtz resonator (a reactive element), and acoustic board B, comprising two layers of dissipative element and a modified Helmholtz resonator (a reactive element). The depth of the acoustic boards was limited to 0.3 m to meet maintenance and operational requirements. To address the limited length of the resonating tube and cavity, a modified Helmholtz resonator was employed, internally extending the resonating tube. By employing acoustic boards A and B and utilizing an *APSO* optimizer and *SA* to link OBJ_1 (case I) and OBJ_2 (case II), the optimal design values were efficiently and easily optimized within the constraints of available space. Simulated results demonstrated that the *APSO* method produced slightly superior optimal solutions compared to the *SA* method. The

importance of the four *APSO* parameters (α, β, p, $iter_{max}$) in achieving accurate solutions during *APSO* optimization was highlighted in Table 3. Moreover, Figs. 15 and 17 showcased the maximized sound absorbing coefficient (α) at the desired frequencies. Furthermore, the effectiveness of the acoustic boards in reducing overall wideband noise at the receiver was evaluated and presented in Tables 4 and 6, as well as Fig. 16. The results indicated that the $L_{p(RV1)}$ at the receiver decreased from 131 dB(A) to 118.2 dB(A) around when acoustic boards A and B were utilized, with a significant reduction in attenuation at 110 Hz. Additionally, Fig. 14-(a), 14-(b), and 14-(c) clearly illustrated the variation in the noise distribution of L_p inside the machine room at a height of 1.0 m with the acoustical boards incorporated, demonstrating the effective elimination of the reverberant component. Notably, Fig. 18 highlighted that acoustic board B provided a broader spectrum of sound attenuation compared to acoustic board A. In conclusion, the employed approach for optimizing the design of shaped acoustical boards within space limitations proved to be efficient, straightforward, and highly effective in achieving the desired acoustical performance.

Acknowledgements

The authors acknowledge the financial support from Tatung University (B113-M06-016), ROC.

Appendix A. Four Pole Transfer Matrix of Sound Absorber A's Dissipative Part

When considering a three-dimensional acoustic wave propagating through a quiescent medium enclosed by rigid rectangular partitions, as depicted in Fig. 2, the governing equation for the wave can be expressed in matrix form [47–50,71]:

$$\left(\frac{\partial^2}{\partial t^2} - c_o^2\nabla^2\right)p = 0 \tag{A1}$$

Using the separation of variables method, the acoustical pressure p and acoustic particle velocity u_z are given as

$$p(x,y,z,t) = \sum_{m=0}^{\infty}\sum_{n=0}^{\infty} k_{z,m,n}\cos\left(\frac{m\pi x}{b}\right)\cos\left(\frac{n\pi y}{h}\right)\begin{pmatrix} C_{1,m,n}e^{-jk_{z,m,n}z} \\ +C_{2,m,n}e^{+jk_{z,m,n}z}\end{pmatrix}e^{i\omega t} \tag{A2}$$

$$u_z(x,y,z,t) = \frac{1}{\rho_o c_o k_o}\sum_{m=0}^{\infty}\sum_{n=0}^{\infty}\cos\left(\frac{m\pi x}{b}\right)\cos\left(\frac{n\pi y}{h}\right)\begin{pmatrix} C_{1,m,n}e^{-jk_{z,m,n}z} \\ +C_{2,m,n}e^{+jk_{z,m,n}z}\end{pmatrix}e^{i\omega t} \tag{A3}$$

where

$$k_{x,m}^2 + k_{y,n}^2 + k_{z,m,n}^2 = k_o^2 \tag{A4}$$

Considering a plane wave at the fundamental mode with (m = 0, n = 0), the wave will propagate if the frequency satisfies the condition $f < \frac{c_o}{2h}$. where h represents the larger transverse dimension of the rectangular partition. In the case of a one-dimensional plane wave propagating perpendicular to a uniform and partitioned section, Equations (A2) and (A3) can be simplified as [47–50,71]:

$$p(z,t) = \left(B_1 e^{-jk_o z} + B_2 e^{+jk_o z}\right)e^{i\omega t} \tag{A5a}$$

$$u(z,t) = \left(\frac{B_1}{\rho_o c_o}e^{-jk_o z} - \frac{B_2}{\rho_o c_o}e^{+jk_o z}\right)e^{i\omega t}$$

Taking the boundary conditions of node 1 (z = 0) and node 2 (z = L) into Eq. (A5) yields [47].

$$\begin{pmatrix} p_1 \\ \rho_o c_o u_1\end{pmatrix} = \begin{bmatrix} 1 & 1 \\ 1 & -1\end{bmatrix}\begin{pmatrix} B_1 \\ B_2\end{pmatrix} \tag{A6a}$$

$$\begin{pmatrix} p_2 \\ \rho_o c_o u_2\end{pmatrix} = \begin{bmatrix} e^{-jk_o L} & e^{+jk_o L} \\ e^{-jk_o L} & -e^{+jk_o L}\end{bmatrix}\begin{pmatrix} B_1 \\ B_2\end{pmatrix} \tag{A6b}$$

Rearranging Eq. (6) yields

$$\begin{pmatrix} p_2 \\ u_2\end{pmatrix} = \begin{bmatrix} cos(k_o L) & jZ_1\, sin(k_o L) \\ j\dfrac{1}{Z_1}sin(k_o L) & cos(k_o L)\end{bmatrix}\begin{pmatrix} p_1 \\ \rho_o c_o u_1\end{pmatrix} \tag{A7}$$

As illustrated in Fig. 3-(a), the acoustical impedance on the perforate front plate is derived from the bottom wall, where the impedance value is infinite. Within the sound field of the sound board (dissipative unit), there are four nodes representing the absorbing impedance. The one-layer dissipative part consists of a "rigid-backing plate + L_1 thickness of air + D_{f1} thickness of acoustical wool + q_1 thickness of the perforate front plate." As deduced in Equation (A7) [47–50,71], which describes the wave propagation in a quiescent medium denoted by "m," the general matrix form between node 1 and node 2 can be expressed as follows:

$$\begin{pmatrix} p_2 \\ u_2\end{pmatrix} = \begin{bmatrix} cos(k_m L) & jZ_m \sin(k_m L) \\ j\dfrac{1}{Z_m}\sin(k_m L) & cos(k_m L)\end{bmatrix}\begin{pmatrix} p_1 \\ u_1\end{pmatrix} \tag{A8}$$

Therefore, the matrix form of the acoustic pressure p and the acoustic particle velocity u between node 0 and node 1 is given as:

$$\begin{pmatrix} p_1 \\ u_1 \end{pmatrix} = \begin{bmatrix} cos(\omega L_1/c_o) & j\rho_o c_o \sin(\omega L_1/c_o) \\ j\dfrac{\sin(\omega L_1/c_o)}{\rho_o c_o} & cos(\omega L_1/c_o) \end{bmatrix} \begin{pmatrix} p_o \\ u_o \end{pmatrix} \tag{A9}$$

where c_o and ρ_o are air's sound speed and density, and L_1 is the depth of the air.

Development of Eq. (A9) yields.

$$Z_1 = -j\rho_o c_o \cot(\omega L_1 / c_o) \tag{A10}$$

The matrix form of the acoustical pressure p and acoustical particle velocity u with regard to node 1 and node 2 is expressed as below:

$$\begin{pmatrix} p_2 \\ u_2 \end{pmatrix} = \begin{bmatrix} cos(k_{fiber1}D_{f1}) & jZ_{fiber1}\sin(k_{fiber1}D_{f1}) \\ j\dfrac{\sin(k_{fiber1}D_{f1})}{Z_{fiber1}} & cos(k_{fiber1}D_{f1}) \end{bmatrix} \begin{pmatrix} p_1 \\ u_1 \end{pmatrix} \tag{A11}$$

Developing Eq. (A11) yields

$$Z_2 \left[= \frac{p_2}{u_2} \right] = Z_{fiber1} \frac{Z_1 cos(k_{fiber1}D_{f1}) + jZ_{fiber1} sin(k_{fiber1}D_{f1})}{Z_1 sin(k_{fiber1}D_{f1}) + Z_{fiber1} cos(k_{fiber1}D_{f1})} \tag{A12}$$

Developing Eq. (A12) using the specific normal impedance together with wave number which was deduced from Delany & Bazley [72] yields

$$Z_2 = (R_{fiber1} + jX_{fiber1}) \cdot$$

$$\frac{Z_1 \begin{bmatrix} cos(k_{11}D_{f1})cosh(k_{12}D_{f1}) \\ -jsin(k_{11}D_{f1})sinh(k_{12}D_{f1}) \end{bmatrix} + \left\{ \begin{bmatrix} -X_{fiber1} sin(k_{11}D_{f1})cosh(k_{12}D_{f1}) \\ +R_{fiber1} sinh(k_{12}D_{f1})cos(k_{11}D_{f1}) \end{bmatrix} + j \begin{bmatrix} R_{fiber1} sin(k_{11}D_{f1})cosh(k_{12}D_{f1}) \\ -X_{fiber1} sinh(k_{12}D_{f1})cos(k_{11}D_{f1}) \end{bmatrix} \right\}}{Z_1 \begin{bmatrix} -sinh(k_{12}D_{f1})cos(k_{11}D_{f1}) \\ +jsin(k_{11}D_{f1})cosh(k_{12}D_{f1}) \end{bmatrix} + \begin{pmatrix} R_{fiber1} \\ +jX_{fiber1} \end{pmatrix} \begin{bmatrix} cos(k_{11}D_{f1})cosh(k_{12}D_{f1}) \\ -jsin(k_{11}D_{f1})sinh(k_{12}D_{f1}) \end{bmatrix}} \tag{A13a}$$

$$k_{11} = \frac{\omega}{c_o}\left[1 + c_1\left(\frac{\rho_o f}{R_1}\right)^{c_2}\right];\ k_{12} = \frac{\omega}{c_o}\left[c_3\left(\frac{\rho_o f}{R_1}\right)^{c_4}\right]$$

$$R_{fiber1} = \rho_o c_o\left[1 + c_5\left(\frac{\rho_o f}{R_1}\right)^{c_6}\right];\ X_{fiber1} = \rho_o c_o\left[c_7\left(\frac{\rho_o f}{R_1}\right)^{c_8}\right] \tag{A13b}$$

where c_1~c_8 are the material constants of the porous acoustical wool, and R_1 is the acoustical wool's acoustical flow resistance.

When sound flows into the perforated plate, it is important to consider that the incident sound passes through the holes of the perforated front plate and immediately transmits to the porous material located behind it. In this process, the particle velocity is minimally reduced [47−50,71]. Based on the characteristic of particle velocity's continuity, it can be expressed as follows:

$$u_2 = u_3 \tag{A14}$$

Acoustic impedance yields

$$p_3 = Z_{p1}u_2 + p_2 \tag{A15}$$

Combining Eq. (A14)~(A15), the transfer matrix between point 2 and point 3 is given as

$$\begin{pmatrix} p_3 \\ u_3 \end{pmatrix} = \begin{bmatrix} 1 & Z_{p1} \\ 0 & 1 \end{bmatrix} \begin{pmatrix} p_2 \\ u_2 \end{pmatrix} \tag{A16}$$

Appendix B. Four Pole Transfer Matrix of Sound Absorber B's Dissipative Part

As shown in Fig. 3-(b), the acoustical impedance on the perforate front plate is derived from the bottom wall, where the impedance value is considered infinite. Within the sound board's sound field, there are seven nodes representing the absorbing impedance. The two-layer sound board (dissipative part) consists of a "rigid-backing plate + L1 thickness of air + D_{f1} thickness of the acoustic wool + q_1 thickness of the perforate front plate + L2 thickness of air + D_{f2} thickness of the acoustic wool + q_2 thickness of the perforate front plate." The matrix

form between node 0~node 1, node 1~node 2, and node 2~node 3 are the same as the derivation in Appendix A. Referring to Equation (A8) in Appendix A, the general matrix form between node 3 and node 4 is given as:

$$\begin{pmatrix} p_4 \\ u_4 \end{pmatrix} = \begin{bmatrix} cos(\omega L_1/c_o) & j\rho_o c_o \, sin\,(\omega L_1/c_o) \\ j\dfrac{sin\,(\omega L_1/c_o)}{\rho_o c_o} & cos(\omega L_1/c_o) \end{bmatrix} \begin{pmatrix} p_3 \\ u_3 \end{pmatrix} \tag{B1}$$

Development of Eq. (B1) yields

$$Z_4 = -j\rho_o c_o \, cot(\omega L_2 / c_o) \tag{B2}$$

The matrix form of the acoustic pressure p and acoustic particle velocity u with regard to node 4 and node 5 is expressed as below:

$$\begin{pmatrix} p_5 \\ u_5 \end{pmatrix} = \begin{bmatrix} cos\left(k_{fiber2}D_{f2}\right) & jZ_{fiber2}\, sin\,\left(k_{fiber2}D_{f2}\right) \\ j\dfrac{sin\,\left(k_{fiber2}D_{f2}\right)}{Z_{fiber2}} & cos\left(k_{fiber2}D_{f2}\right) \end{bmatrix} \times \begin{pmatrix} p_4 \\ u_4 \end{pmatrix} \tag{B3}$$

Developing Eq. (B3) yields

$$Z_5\left[=\frac{p_5}{u_5}\right] = Z_{fiber4}\frac{Z_4\, cos\left(k_{fiber2}D_{f2}\right) + jZ_{fiber2}\, sin\,\left(k_{fiber2}D_{f2}\right)}{Z_4\, sin\left(k_{fiber2}D_{f2}\right) + Z_{fiber2}\, cos\,\left(k_{fiber2}D_{f2}\right)} \tag{B4}$$

Developing Eq. (B4) using the specific normal impedance and wave number which was deduced from Delany & Bazley [72] yields

$$Z_5 = \left(R_{fiber2} + jX_{fiber2}\right)\cdot$$

$$k_{21} = \frac{\omega}{c_o}\left[1 + c_1\left(\frac{\rho_o f}{R_2}\right)^{c_2}\right];\; k_{22} = \frac{\omega}{c_o}\left[c_3\left(\frac{\rho_o f}{R_2}\right)^{c_4}\right]$$

$$R_{fiber2} = \rho_o c_o\left[1 + c_5\left(\frac{\rho_o f}{R_2}\right)^{c_6}\right];\; X_{fiber2} = \rho_o c_o\left[c_7\left(\frac{\rho_o f}{R_2}\right)^{c_8}\right] \tag{B5b}$$

where c_1 to c_8 represent the material constants of the porous acoustic wool. When sound flows into the perforated plate, it is important to consider that the incident sound passes through the holes of the perforated plate and immediately transmits to the porous material located behind it. In this process, the particle velocity experiences minimal reduction [47−50,71]. This can be attributed to the characteristic of particle velocity's continuity, and it can be expressed as follows:

$$u_5 = u_6 \tag{B6}$$

Acoustic impedance yields

$$p_6 = Z_{p2}u_5 + p_5 \tag{B7}$$

Combining Eqs. (B6)~(B7), the transfer matrix between point 5 and point 6 is given as

$$\begin{pmatrix} p_6 \\ u_6 \end{pmatrix} = \begin{bmatrix} 1 & Z_{p2} \\ 0 & 1 \end{bmatrix} \begin{pmatrix} p_5 \\ u_5 \end{pmatrix} \tag{B8}$$

$$Z_4\begin{bmatrix} cos\left(k_{21}D_{f2}\right)cosh\left(k_{22}D_{f2}\right) \\ -jsin\left(k_{21}D_{f2}\right)sinh\left(k_{22}D_{f2}\right) \end{bmatrix} + \left\{ \begin{array}{l} -\begin{bmatrix} X_{fiber2}\, sin\left(k_{21}D_{f2}\right)cosh\left(k_{22}D_{f2}\right) \\ +R_{fiber2}\, sinh\left(k_{22}D_{f2}\right)cos\left(k_{21}D_{f2}\right) \end{bmatrix} \\ +j\begin{bmatrix} R_{fiber2}\, sin\left(k_{21}D_{f2}\right)cosh\left(k_{22}D_{f2}\right) \\ -X_{fiber2}\, sinh\left(k_{22}D_{f2}\right)cos\left(k_{21}D_{f2}\right) \end{bmatrix} \end{array} \right\}$$
$$\overline{Z_4\begin{bmatrix} -sinh\left(k_{22}D_{f2}\right)cos\left(k_{21}D_{f2}\right) \\ +jsin\left(k_{21}D_{f2}\right)cosh\left(k_{22}D_{f2}\right) \end{bmatrix} + \begin{pmatrix} R_{fiber2} \\ +jX_{fiber2} \end{pmatrix}\begin{bmatrix} cos\left(k_{21}D_{f2}\right)cosh\left(k_{22}D_{f2}\right) \\ -jsin\left(k_{21}D_{f2}\right)sinh\left(k_{22}D_{f2}\right) \end{bmatrix}} \tag{B5a}$$

References

[1] Tong H, Kang J. Relationships between noise complaints and socio-economic factors in England. Sustain Cities Soc 2021; 65:102573.

[2] Bolognese M, Fidecaro F, Licitra G, Palazzuoli D, Fredianelli L. Port noise impact and citizens' complaints evaluation in RUMBLE and Mon ACUMEN INTERREG projects. Proceedings of the 26th international congress on sound and vibration. Montreal, QC: Canada; 2019.

[3] Muzet A. Environmental noise, sleep and health. Sleep Med Rev 2007;11:135−42.

[4] Erickson Lucy C, Newman Rochelle S. Influences of background noise on infants and children. Curr Dir Psychol Sci 2017;26(5):451−7.

[5] Dratva J, Phuleria HC, Foraster M, Gaspoz JM, Keidel D, Kunzli N, et al. Transportation noise and blood pressure in a

population-based sample of adults. Environ Health Perspect 2012;120(1):50−5.
[6] Van Kempen E, Babisch W. The quantitative relationship between road traffic noise and hypertension: a meta-analysis. J Hypertens 2012;30(6):1075−86.
[7] Bluhm GL, Berglind N, Nordling E, Rosenlund M. Road traffic noise and hypertension. Occup Environ Med 2007; 64(2):122−6.
[8] Petri D, Licitra G, Vigotti MA, Fredianelli L. Effects of exposure to road, railway, airport and recreational noise on blood pressure and hypertension. Int J Environ Res Publ Health 2021;18(17):9145.
[9] Lee PJ, Park SH, Jeong JH, Choung T, Kim KY. Association between transportation noise and blood pressure in adults living in multistorey residential buildings. Environ Int 2019; 132:105101.
[10] Vukić L, Mihanović V, Fredianelli L, Plazibat V. Seafarers' perception and attitudes towards noise emission on board ships. Int J Environ Res Publ Health 2021;18(12):6671.
[11] Rossi L, Prato A, Lesina L, Schiavi A. Effects of low-frequency noise on human cognitive performances in laboratory. Build Acoust 2018;25(1):17−33.
[12] Miedema HME, Oudshoorn CGM. Annoyance from transportation noise: relationships with exposure metrics DNL and DENL and their confidence intervals. Environ Health Perspect 2001;109:409−16.
[13] Licitra G, Fredianelli L, Petri D, Vigotti MA. Annoyance evaluation due to overall railway noise and vibration in Pisa urban areas. Sci Total Environ 2016;568:1315−25.
[14] Fredianelli L, Carpita S, Licitra G. A procedure for deriving wind turbine noise limits by taking into account annoyance. Sci Total Environ 2019;648:728−36.
[15] Redel-Macõas MD, Woodcock JS, Waddington DC. Subjective rating and assessing environmental sound of an industrial nature with tonal and impulsive characteristics. In: INTER-NOISE and NOISE-CON congress and conference proceedings. Institute of Noise Control Engineering; 2019. p. 5019−27.
[16] Marquis-Favre C, Braga R, Gourdon E, Combe C, Gille LA, Ribeiro C, et al. Estimation of psychoacoustic and noise indices from the sound pressure level of transportation noise sources: investigation of their potential benefit to the prediction of long- term noise annoyance. Appl Acoust 2023;211: 109:56.
[17] Lavandier C, Regragui M, Dedieu R, Royer C, Can A. Influence of road traffic noise peaks on reading task performance and disturbance in a laboratory context. Acta Acustica 2022;6:3.
[18] Huth C, Forstreuter M, Arlt R, Liepert M. Annoyance at the point of emission versus immission for impulsive noises at train passings. J Acoust Soc Am 2020;148(4 Supplement): 2567.
[19] Tao Y, Chai Y, Kou L, Kwan MP. Understanding noise exposure, noise annoyance, and psychological stress: incorporating individ- ual mobility and the temporality of the exposure-effect relationship. Appl Geogr 2020;125(102):28.
[20] Kukulski B, Wszolek T. Development of parameter-based criteria for applying adjustment for highly impulsive sound sources. Appl Acoust 2022;185(108):37.
[21] Virjonen P, Hongisto V, Radun J. Annoyance penalty of periodically amplitude-modulated wide-band sound. J Acoust Soc Am 2019;146(6):4159−417.
[22] Rajala V, Hongisto V. Annoyance penalty of impulsive noise − the effect of impulse onset. Build Environ 2020;168:106:53.
[23] Licitra G, Bolognese M, Chiari C, Carpita S, Fredianelli L. Noise source predominance map: a new representation for strategic noise maps. Noise Mapp 2022;9(1):269−79.
[24] Merchant ND, Blondel P, Dakin DT, Dorocicz J. Averaging underwater noise levels for environmental assessment of shipping. J Acoust Soc Am 2012;132(4):EL343−9.
[25] Kellett P, Turan O, Incecik A. A study of numerical ship underwater noise prediction. Ocean Eng 2013;66:113−20.
[26] Erbe C, Smith JN, Redfern JV, Peel D. Impacts of shipping on marine fauna. Front Mar Sci 2020;7:637.
[27] Bittencourt L, Carvalho RR, Lailson-Brito J, Azevedo AF. Underwater noise pollution in a coastal tropical environment. Mar Pollut Bull 2014;83(1):331−6.
[28] Bernardini M, Fredianelli L, Fidecaro F, Gagliardi P, Nastasi M, Licitra G. Noise assessment of small vessels for action planning in canal cities. Environments 2019;6:31.
[29] Fredianelli L, Nastasi M, Bernardini M, Fidecaro F, Licitra G. Pass-by characterization of noise emitted by different categories of seagoing ships in ports. Sustainability 2020;12(5): 1740.
[30] Nastasi M, Fredianelli L, Bernardini M, Teti L, Fidecaro F, Licitra G. Parameters affecting noise emitted by ships moving in port areas. Sustainability 2020;12(20):8742.
[31] Badino A, Borelli D, Gaggero T, Rizzuto E, Schenone C. Airborne noise emissions from ships: experimental characterization of the source and propagation over land. Appl Acoust 2016;104:158−71.
[32] Borelli Davide. Maritime airborne noise: ships and harbours. Int J Acoust Vib 2019;24(4):631.
[33] Schiavoni S, D'Alessandro F, Borelli D, Fredianelli L, Gaggero T, Schenone C, et al. Airborne sound power levels and spectra of noise sources in port areas. Int J Environ Res Publ Health 2022;19(17):10996.
[34] Fredianelli L, Gaggero T, Bolognese M, Borelli D, Francesco F, Schenone C, et al. Source characterization guidelines for noise mapping of portareas. Heliyon 2022;8(3): e09021.
[35] Fredianelli L, Bolognese M, Fidecaro F, Licitra G. Classification of noise sources for port area noise mapping. Environments 2021;8(2):12.
[36] Di Bella Antonino, Remigi Francesca. Prediction of noise of moored ships. Acoustical Society of America. In: Proceedings of Meetings on Acoustics ICA2013. 19; 2013.
[37] Vukić L, Peronja I, Mandić N. Significance and current regulations of external airborne noise from ships. WIT Trans Built Environ 2022;212:139−48.
[38] Vukić L, Peronja I, Glavinović R. Multi-faceted analysis of airborne noise impact in the port of split (I). J Mar Sci Eng 2022;10(10):1564.
[39] Bolognese M, Fidecaro F, Licitra G, Palazzuli D. Port noise impact and citizens' complaints evaluation in RUMBLE and Mon ACUMEN INTERREG projects. Proceedings of the 26th international congress on sound and vibration. Montreal, QC: Canada; 2019.
[40] Kanka S, Fredianelli L, Artuso F, Fidecaro F, Licitra G. Evaluation of acoustic comfort and sound energy transmission in a yacht. Energies 2023;16(2):808.
[41] Borelli D, Gaggero T, Rizzuto E, Schenone C. Onboard ship noise: acoustic comfort in cabins. Appl Acoust 2021; 177(2021):107912.
[42] Borelli D, Gaggero T, Schenone C. Analysis of noise on board a ship during navigation and manoeuvres. Ocean Eng 2015;105:256−69.
[43] Hong HS, Sang RS, Han HS. Developing the logic for evaluating the indoor noise of a naval vessel using a back-propagation neural network. J Mech Sci Technol 2011;25:2755−62.
[44] Bocanegra JA, Borelli D, Gaggero T, Rizzuto E, Schenone C. Characterizing onboard noise in ships: insights from statistical, machine learning and advanced noise index analyses. Ocean Eng 2023;285:115273.
[45] Chiu MC. Noise elimination of a multi-tone noise for a space constrained room lined with hybrid sound absorbers using a particle swarm method. J Mech Sci Technol 2014;28(9):1−13.
[46] Duan H, Shen X, Wang E, Yang F, Zhang XN, Yin Q. Acoustic multi-layer Helmholtz resonance metamaterials with multiple adjustable absorption peaks. Appl Phys Lett 2021;118:241904. 1-5.
[47] Chang YC, Yeh LJ, Chiu MC. Optimization of constrained multi-layer absorbers by using genetic algorithms. Int J Acoust Vib 2004;9(4):175−85.

[48] Chang YC, Yeh LJ, Chiu MC. Optimization of composite absorbers on constrained sound reverberant system by using simulated annealing. Appl Acoust 2005;66:341−52.
[49] Chang YC, Yeh LJ, Chiu MC. Optimization of double-layer absorbers on constrained sound absorption system by using genetic algorithm. Int J Numer Methods Eng 2005;62: 317−33.
[50] Chang YC, Yeh LJ, Chiu MC, Lai GJ. Shape optimization on constrained single-layer sound absorber by using GA method and mathematical gradient methods. J Sound Vib 2005;286(4−5):941−61.
[51] Chiu MC, Chang YC, Lan TS, Chen HS. Optimization of circular mufflers equipped with multiple reverse chambers at high-order-modes using the GA method. J Mar Sci Technol 2022;30(6):322−39.
[52] Lan TS, Chiu MC. Optimal noise control on plant using simulated annealing. Trans Can Soc Mech Eng 2008;32(3−4): 423−4382008.
[53] Chiu MC. Optimization of equipment allocation and sound-barriers shape in a multi-noise plant by using simulated annealing. Noise Vib Worldw 2009;40(7):23−35.
[54] Chiu MC, Cheng HC. Optimal design of multi-diffuser mufflers using simulated annealing method. Arch Acoust Q 2021;46(4):685−96.
[55] Chiu MC. Shape optimization of multi-chamber tube-extended mufflers within specified back pressures using a particle swarm method. Noise Vib Worldw 2013;44(3):10−23.
[56] Chiu MC. Noise abatement in reverberant sound field by using a particle swarm method. Build Acoust 2013;20(1): 1−24.
[57] Beranek LL, Ver IL. Noise and vibration control engineering. New York: John Wiley & Sons; 1992.
[58] Munjal ML. Acoustics of ducts and mufflers with application to exhaust and ventilation system design. New York: John Wiley & Sons; 1987.
[59] Bies DA, Hansen CH. Engineering noise control. UK: Unwin Hyman; 1988.
[60] Lord JW, Rayleigh S. The theory of sound. New York: Dover Publicaions, Inc.; 1945.
[61] Chang YC, Yeh LJ, Chiu MC. Optimization of composite absorbers on constrained sound reverberant system by using simulated annealing. Appl Acoust 2005;66:341−52.
[62] Chiu MC, Lan TS. Noise source identification in sound field by using simulated annealing. Acta Acustica united Acustica 2007;93:486−97.
[63] Kennedy J, Eberhart RC. Particle swarm optimization. Proc. IEEE Conf. Neural Networks IV 1995;4:1942−8.
[64] Kennedy J, Eberhart RC. Particle swarm optimization. Piscataway, NJ. In: Proc. Of IEEE international conference on neural networks; 1995. p. 1942−8.
[65] Kennedy J, Eberhart RC. Swarm intelligence. Academic Press; 2001.
[66] Yang XS, Deb S, Fong S. Accelerated particle swarm optimization and support vector machine for business optimization and applications, conference paper in communications in computer and information science. 2012.
[67] Yang XS. Nature-inspired metaheuristic algorithms. Luniver Press; 2008.
[68] Yang XS. Engineering optimization: an introduction with metaheuristic applications. John Wiley & Sons; 2010.
[69] Metropolis A, Rosenbluth W, Rosenbluth MN, Teller H, Teller E. Equation of static calculations by fast computing machines. J Chem Phys 1953;21:1087−92.
[70] Kirkpatrick S, Gelatt CD, Vecchi MP. Optimization by simulated annealing. Science 1983;220:671−80.
[71] Chiu MC, Yeh LJ, Chang YC, Lai GJ. Computer aided design on perforated single-layer absorbers under space constraints. Int J Adv Manuf Technol 2007;32(5−6):537−46.
[72] Delany ME, Bazley EN. Acoustical properties of fibrous absorbent materials. Appl Acoust 1969;13:105−16.